Regulating HER and OER performances of 2D materials by the external physical fields

Chunling Qin[1], Shuang Chen[1], Hassanien Gomaa[1,4], Mohamed A. Shenashen[3], Sherif A. El-Safty[3], Qian Liu[5], Cuihua An[1,*] Xijun Liu[2,*] Qibo Deng[1,7*] Ning Hu[1,6]

[1] School of Mechanical Engineering, and School of Materials Science and Engineering, Hebei University of Technology, Tianjin 300401, China.

[2] State Key Laboratory of Featured Metal Materials and Life-cycle Safety for Composite Structures, Guangxi Key Laboratory of Processing for Non-Ferrous Metals and Featured Materials, School of Resources, School of Resources, Environment and Materials, Guangxi University, Nanning 530004, China.

[3] Research Center for Macromolecules and Biomaterials, National Institute for Materials Science (NIMS), 1-2-1 Sengen, Tsukuba-shi, Ibaraki-ken 305-0047, Japan.

[4] Department of Chemistry, Faculty of Science, Al-Azhar University, Assiut 71524, Egypt.

[5] Institute for Advanced Study, Chengdu University, Chengdu 610106, Sichuan, China.

[6] State Key Laboratory of Reliability and Intelligence Electrical Equipment, Hebei University of Technology, Tianjin, 300130, China.

[7] Advanced Equipment Research Institute Co., Ltd. Of HEBUT, Tianjin, 300401, China.

*Corresponding author. Cuihua An (ancuihua@hebut.edu.cn); Xijun Liu (xjliu@gxu.edu.cn); Qibo Deng (qibodeng@hebut.edu.cn)

Abstract: Hydrogen fuel has long been regarded as a promising and viable alternative to conventional fossil fuels for ensuring our energy landscape of the future. The electro-catalytic water splitting represents a sustainable and eco-friendly technology for the efficient and abundant production of high-purity hydrogen on a large scale. The practical applications of the technology require the improvement in the reaction kinetics of the hydrogen evolution reaction (HER) at the anode and the oxygen evolution reaction (OER) at the cathode. Additionally, the continual optimization of the catalyst's catalytic activity and structural stability is crucial for the practical implementation of this technology. Two-dimensional (2D) nanomaterials play a crucial role in electrocatalysis due to their unique physicochemical properties and abundance of active sites. The roles and mechanisms of the external physical field assistance on the HER and OER have attracted increasing attention. The external factors, such as electric field, magnetic field, strain, light, temperature, and ultrasound, can be applied to the process of synthesis and electrocatalysis. In this paper, the research on the synthesis of physical field-assisted electrolytic water catalysts is summarized. Then, recent advances in the field-assisted HER and OER are introduced classification by different mechanisms. Finally, the paper points out the key challenges and prospects of the rapidly developing research field.

Key Words: External physical fields; HER; OER; Preparation; 2D materials

外加物理场调控二维材料的 HER 和 OER 性能

秦春玲[1]，陈爽[1]，Hassanien Gomaa[1]，Mohamed A. Shenashen[3]，Sherif A. El-Safty[3],刘倩[5]，安翠华[1,*]，刘熙俊[2,*]，邓齐波[1,7*]，胡宁[1,6]

1 河北工业大学机械工程学院，材料科学与工程学院，天津 300401

2 广西大学资源环境与材料学院，广西有色金属及特色材料加工重点实验室，广西有色金属及特色材料

加工重点实验室，南宁 53004
3 日本国立材料科学研究所大分子与生物材料研究中心，筑波 305-0047
4 埃及爱资哈尔大学理学院，阿斯尤特，71524
5 河北工业大学省部共建电工装备可靠性与智能化国家重点实验室，天津 300130
6 河北工业大学高端装备与结构技术研究院，天津 300401

摘要：长期以来，氢燃料一直被认为是一种有前途和可行的传统化石燃料的替代品，以确保我们未来的能源格局。电催化水分解是一种可用于大规模高效生产高纯度氢气的可持续和环保的技术。该技术的实际应用需要提高两个电极上的析氢反应（HER）和析氧反应（OER）的反应动力学。此外，催化剂催化活性和结构稳定性的持续优化对于该技术的实际实施至关重要。二维（2D）纳米材料由于其独特的物理化学性质和丰度的活性位点在电催化中起着至关重要的作用。外加物理场在辅助改善 HER 和 OER 方面的作用和机制越来越受到关注。外部因素，如电场，磁场，应变，光，温度和超声波，可以应用于合成和电催化过程。本文综述了物理场辅助电解水催化剂的合成研究。随后，根据作用机制的不同，对外场辅助 HER 和 OER 的研究进行了分类。最后，本文指出了本领域快速发展所面临的主要挑战和前景。
关键词：外加物理场；析氢反应；析氧反应；合成；二维材料

1 Introduction

The surging requirements for energy and growing ecological damage have led to the innovation and usage of the clean energy sources as a mean to minimize the use of fossil fuels [1-3]. With its exceptional energy density (142 MJ/kg) and advantage as a carbon-free energy carrier, hydrogen is widely regarded as a highly promising candidate to supplant fossil fuels in the future [4-8]. Producing green hydrogen energy through water electrolysis is a simple, efficient, and clean approach [9]. Whereas, both the anode and cathode half-reactions, namely the OER and HER, necessitate a supernumerary input of energy called the overpotential to overcome the reaction resistance [10,11]. Therefore, it is of utmost importance to carefully select the appropriate catalyst. The noble metal platinum is generally acknowledged as the most efficient HER electrocatalyst in acidic environments, while iridium and ruthenium are widely acknowledged as the best OER electrocatalysts in alkaline environments [12-19]. Nevertheless, the exorbitant expense and rareness of the precious metals present a challenge to the industrialization of the electrolytic water technology. Thus, it becomes crucial to decrease the content of the noble metals while upholding the exceptional electrocatalytic performances or explore alternative catalysts based on the non-noble metals that exhibit comparable performance to the noble metal-based counterparts. With the continuous breakthroughs of nanomaterial production technology, low-dimensional nanomaterials have become a hotspot for electrocatalysts due to their unique structure, excellent electronic structure, and physicochemical properties.

2D materials are materials with a size of 1-100 nm in one dimension, typically exhibiting a sheet-like structure [20]. The commonly utilized 2D electrocatalysts include 2D metal carbides (MXene) [21,22], 2D metal materials [23-26], double hydroxides (LDHs) [27-29], 2D metal-organic frameworks [30], single-atom catalysts supported on 2D materials [31-34], transition metal sulfides (TMDs) [35,36],

graphene and so on. Due to their atomic-scale thickness, these materials offer a substantial specific surface area, abundant high-activity sites, and exceptional efficacy in facilitating electrons transfer, and have extraordinary performance in the electrolytic water reaction. Furthermore, they also possess easy modification properties via using traditional methods such as forming heterojunctions or homojunctions, element doping [37,38], introducing defects such as vacancies, changing morphologies and structures, compounding various materials [39-41], and molecular modification. Whereas, these regulation methods mainly focus on the electrocatalyst itself and offer limited improvement in HER and OER performances. Moreover, once synthesized, the performances of electrocatalysts are fixed and difficult to control. Consequently, researchers have now turned their attention to the regulation of the physical fields on electrocatalysis.

Moreover, the external fields utilized for the material synthesis process usually include microwave, ultrasonic, and magnetic fields. The ultrasonic waves are widely applied for physically stripping 2D nanosheets. In comparison to other heating methods such as the tube furnace, microwave heating can uniformly heat materials, and the heating time is shorter. The physical fields utilized in the auxiliary electrocatalysis mainly comprise of magnetic field, light, strain, electric field, temperature field, and ultrasound. For instance, an electric field generated by a gate voltage of 5 V noticeably reduces the overpotential from 240 mV to 38 mV@100 $mA \cdot cm^{-2}$ for a single MoS_2 nanosheet device [42]. It can be observed that the HER performances of the MoS_2 with the assistance of the electric field are significantly improved. It even surpasses the HER performances of the commercially available Pt/C, which is unlikely to be accomplished through the traditional modification approaches. In another example, when a magnetic field with an intensity of 200 mT is applied [43], the OER overpotential of NiFe LDHs can reach 207 mV@10 $mA \cdot cm^{-2}$. Under the physical fields, both the OER and HER performances can be markedly enhanced. The varied materials can be regulated, indicating that external field regulation the electrocatalysis is universal. Furthermore, these enhancements are reversible. In summary, this is a promising, easy-to-manipulate, and universal approach for regulating the electrocatalytic performances that offers the additional freedom in designing catalysts with the outstanding performances.

In this paper, we present a systematic overview of the impacts of diverse physical fields on 2D electrocatalysts. Specifically, we investigate the influences of magnetic field, light, strain, the electric field, temperature, ultrasound, and microwave on the HER and OER efficiencies of 2D materials throughout the synthesis and electrocatalytic processes. The studies on field-assisted electrocatalysis in recent years are classified, according to the mechanisms of influence on the electrocatalytic activity of 2D nanomaterials. Moreover, we emphasize the primary obstacles encountered by the swiftly advancing research field and examine the prospects for future advancements in this area.

2 Physical field-assisted material synthesis

Ultra-thin 2D materials could be synthesized through methods such as water/solvothermal and chemical vapor deposition (CVD). Despite some successes have been achieved, these methods still have limitations. To overcome these limitations, additional degrees of freedom, such as physical fields, need to be introduced. This chapter focuses on studying the effects of the physical fields (Ultrasound, microwave, and magnetic field) on the preparation of 2D catalysts through both top-down and bottom-up synthesis techniques.

2.1 Ultrasound

The methods for synthesizing 2D materials can be categorized into the top-down and bottom-up techniques [44]. The top-down strategy involves the rational use of external forces to delicately separate 2D fragments from the bulk materials [45]. This method is primarily employed for the materials held together by the van der Waals forces, such as layered materials [46]. Ultrasound-assisted peeling of 2D nanosheets is a widely utilized way. For instance, 2D Co-BDC/MoS_2 Hybrid nanosheets (BDC is 1, 4-benzenedicarboxylate) were produced via this method [47]. The Co-BDC facilitates the dissociation of water and intensifies the HER performances of MoS_2 in an alkaline environment. In another work, 2D metal-organic framework (MOF) nanosheets were exfoliated through the ultrasound to address the inadequate OER performances of the bulk MOF [48]. Ultrasonic waves were employed to control the exposure of the dominant facets, resulting in abundant catalytic sites to promote the OER performances. The Tafel slope of the ultrasonically exfoliated Co-MOF nanosheets is 75.71 $mV \cdot dec^{-1}$. Similarly, the controlled synthesis of 2D nickel-cobalt phosphide (NiCoP) with a thickness of 0. 98 nm was achieved [49]. High-frequency ultrasonic waves generate cavitation bubbles, which lead to the formation of the ultra-thin quasi-monolayer $NiCo(OH)_2$ through the high-speed micro-jet and shock wave effects. Then, the 2D quasi-monolayer NiCo phosphide with crystal-amorphous interface was obtained by the phosphating treatment. The HER and OER overpotentials of NiCoP in an alkaline environment are 84 and 259 mV@10 $mA \cdot cm^{-2}$, respectively.

As a typical layered material, MoS_2 can be exfoliated with the assistance of ultrasonication. However, the exfoliated nanosheets exhibit poorly electrocatalytic performances and tend to aggregate easily. But, through the utilization of surfactants and ethanol, the exfoliation method was improved [50]. The exfoliated MoS_2 nanosheets show a decreased HER overpotential of 93 mV@10 $mA \cdot cm^{-2}$, compared to the bulk MoS_2. It is important to note that the types of the layered solvent also affect the effectiveness of the ultrasound-assisted exfoliation. Moreover, the significance of the appropriate layered solvents and ultrasound in the separation of 2D MOF nanosheets was demonstrated in another work [51]. 2D coordination polymers with high HER activity and uniform size stability were prepared.

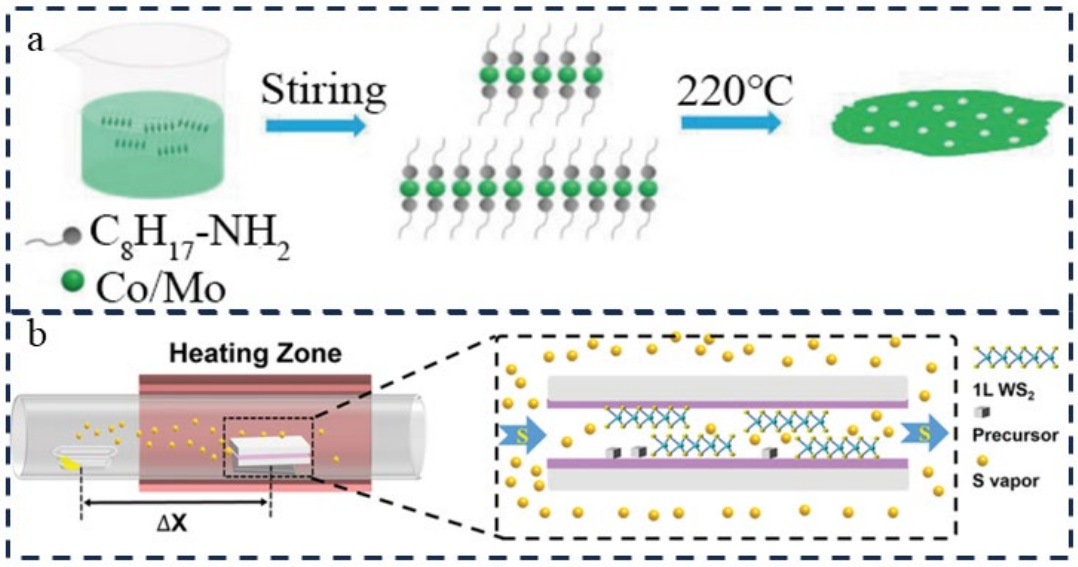

Fig. 1 (a) Schematic diagram of 2D mesoporous Mo_x-Co-O nanosheets prepared by hydrothermal method. Reprinted with permission from Ref. 52. Copyright © 2022, Springer Nature. (b) Improved CVD experimental diagram for realizing the controllable growth of 2D WS_2. Reprinted with permission from Ref. 53. Copyright © 2022, John Wiley and Sons.

2.2 Magnetic field

The bottom-up synthesis strategy involves the utilization of physical and chemical methods to assemble atoms or molecules into 2D materials. This technique can be applied to both the layered and non-layered materials. The bottom-up synthesis approaches are mostly chemical in nature, which include the water/solvothermal method and CVD. For instance, the solvothermal method was used to synthesize mesoporous Mo_x-Co-O hybrid nanosheets that contain both the crystalline and amorphous phases (Fig. 1a) [52]. By adjusting the molar ratio of Mo/Co, the size, mesoporous size, and defect concentration of the nanosheets can be varied. The mesoporous morphology patently amplifies the electrochemically active region of the Mo_x-Co-O nanosheets and the adsorption of intermediates is optimized because of Mo doping and abundant oxygen vacancies, which enhance the OER performances. The 2D mesoporous Mo_x-Co-O nanosheets have an OER overpotential of 276 mV@10 mA·cm^{-2}. For CVD, it can be used to prepare single-atom-scale thin TMDs nanosheets. However, fully controlling their formation is challenging due to the violent evaporation of metal and chalcogenide precursors at the high temperatures and large diffusion rate difference. However, the controllable growth of 2D materials was achieved through the modified CVD technique [53]. The free regulation of the gas phase ratio of the metal precursor to the chalcogenide precursor is accomplished by the two superimposed substrates (Fig. 1b). By modifying the gas phase ratio, size, number of layers, the lateral/vertical heterojunction WS_2 nanosheets can be precisely fabricated. The synthesized MoS_2/WS_2 lateral heterojunction has the excellent HER activity.

Temperature is a commonly important variable for both techniques. The effect of temperature on the synthesis of MoS_2 by molten salt-assisted CVD was studied [54]. It was found that the morphology of MoS_2 sheets changed from dense

triangles to fractal dendrites with an increase in temperature. This change in morphology indirectly affects the formation of MoS_2 with different morphologies, which in turn affect the HER performances. The bottom-up synthesis strategy is more commonly utilized than the top-down synthesis strategy in synthesizing various types of 2D catalysts. Therefore, next, we will introduce the combination of the physical fields and bottom-up synthesis strategy.

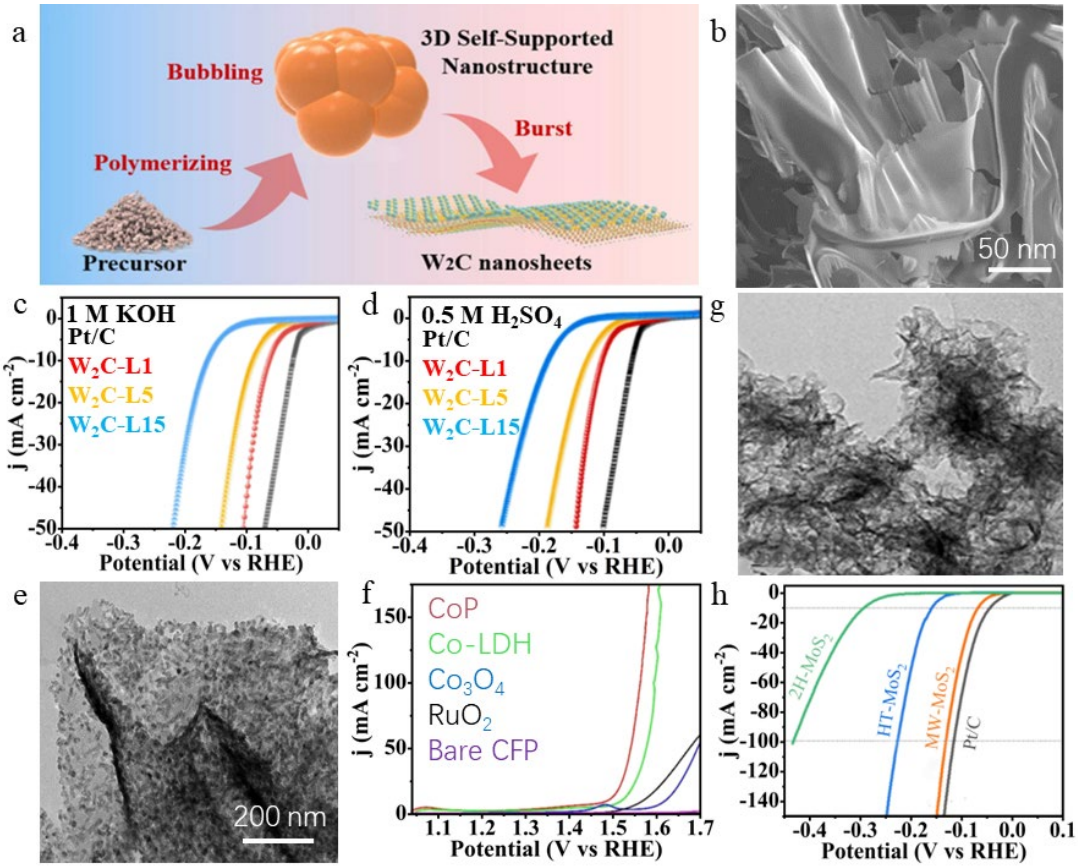

Fig. 2 (a) Schematic diagram of W_2C nanosheets prepared by the microwave-pulse sugar-blowing method. (b) SEM image of the W_2C nanosheets. HER polarization curves in 0.5 M H_2SO_4 (c) and in 1 M KOH (d), W_2C-L1, W_2C-L5 and W_2C-L15 are nanosheets with thickness of 1 nm, 5 nm and 15 nm, respectively. Reprinted with permission from Ref. 58. Copyright © 2022, Elsevier. (e) TEM image of CoP nanosheets. (f) OER polarization curves. Reprinted with permission from Ref. 60. Copyright © 2019, Wiley-VCH Verlag GmbH (g) TEM image of MW-MoS_2. (h) HER polarization curves, HT-MoS_2 and MW-MoS_2 are 1T-MoS_2 prepared by hydrothermal method and microwave method, respectively. Reprinted with permission from Ref. 61. Copyright © 2023, Royal Society of Chemistry.

The magnetic field-assisted self-assembly of magnetic nanoparticles (NPs) has garnered significant attention for its remarkable function. However, the impact of the magnetic field on catalyst synthesis extends beyond this. In particular, 1T-MoS_2 with high conductivity exhibits superior HER performances compared to that of 2H-MoS_2. Yet, the synthesis of pure 1T-MoS_2 had remained a daunting challenge because of its low stability. Fortunately, pure 1T-MoS_2 could be successfully produced via a hydrothermal technique under the influence of a high-intensity magnetic field [55]. The HER overpotential of 1T-MoS_2 created by the magnetic-hydrothermal method measures at 189 mV@10 mA·cm^{-2}. Meanwhile, the magnetic field-induced magnetocaloric effect holds immense potential for heating,

enabling faster heating rates and lower energy consumption than the traditional methods. By the combination of the magnetocaloric effect heating and rapid cooling, the amorphous phase catalysts with rich defects can be easily and rapidly generated. The NiFe LDH prepared by this principle had the remarkable OER performances [56], displaying an overpotential of 246 mV@10 mA·cm^{-2}.

2.3 Microwave

With its high penetrating capability, microwave is able to quickly and evenly heat materials, thus decreasing the heating time [57]. For example, a method for synthesizing ultra-thin W_2C nanosheets involves the microwave-pulse sugar-blowing [58]. As depicted in Fig. 2a, upon the high-energy microwave heating, the glucose firstly undergoes a reaction to form a polymer that takes on a soft gelatinous state. Next, under the action of the gas released by the thermal decomposition of ammonium chloride, the polymer produces a stress relaxation effect and forms a 3D bubble structure. Following, as the bubbles expand, surface tension results in thinner bubble walls. Then, the ultra-thin bubbles graphitize over time, reacting with metal precursors to form carbides. Finally, the carbide bubble structure is then disrupted by microwave, leading to the formation of 2D W_2C nanosheets (Fig. 2b). And the whole synthesis process takes no more than 2 minutes. The HER overpotential of W_2C nanosheets decreases as the thickness of the nanosheets decreases. The overpotential of W_2C-L1 is 64 mV@10 mA·cm^{-2} in 0.5 M H_2SO_4 (Fig. 2c) and 102 mV@10 mA·cm^{-2} in 1 M KOH (Figure 2d).

The introduction of microwave promotes the making of the wrinkled nanosheets. The presence of a wrinkled morphology significantly enhances the HER and OER performances. So 2D $MoTe_2$ nanosheets prepared by microwave had the excellent HER activity [59]. Ultrathin CoP nanosheets with the mesoporous structures (Fig. 2e) were prepared by using CVD and microwave-assisted synthesis [60]. The OER overpotential of the mesoporous CoP nanosheets is 265 mA cm^{-2} (Fig. 2f). Similarly, a rapid high-pressure microwave method was utilized for one-step preparation of 1T-MoS_2 catalysts [61], resulting in twisted nanosheets (Fig. 2g). The HER overpotential of the prepared 1T-MoS_2 is -62 mV@10 mA cm^{-2} (Fig. 2h). In an additional study, 2D nanostructured nickel-iron selenide on nickel foam (NF) was successfully fabricated through the conjunction of electrochemical deposition and microwave [62]. The mixed valence state of nickel (Ni^{2+}/Ni^{3+}) and the high valence state of selenium are produced, which gives the catalyst excellent OER performances in alkaline solution.

3 The impact of external physical fields on electrocatalysis

In the HER and OER processes, various factors such as adsorption free energy, bubbles, mass transfer rate, charge transfer rate, and carrier density exert a major influence on determining the electrocatalytic performances [63]. The physical fields affecting the material preparation and consequently impacting the performance are introduced earlier in this article. It can also have a direct impact on the aforementioned factors during the HER or OER process, thereby optimizing the electrocatalytic performances [64]. Physical fields such as magnetic field, light field, strain, electric field, temperature, ultrasound, are involved in electrocatalysis. This

chapter will primarily focus on the influences and mechanisms of the physical fields on the HER and OER properties of 2D materials.

3.1 The impact of magnetic field on electrocatalysis

The low electrocatalytic efficiency is often caused by the bubbles and a slow mass transfer rate. The studies on the magnetic field-assisted electrocatalysis have demonstrated that the magnetic field can boost mass transfer and promote the detachment of the bubbles from the electrode [43]. Additionally, the magnetocaloric effect, spin regulation of electrons by the magnetic field, and magnetoresistance effect can also be combined with the electrochemical process to optimize HER and OER performances.

3.1.1. The impact of Magnetohydrodynamic convection on electrocatalysis

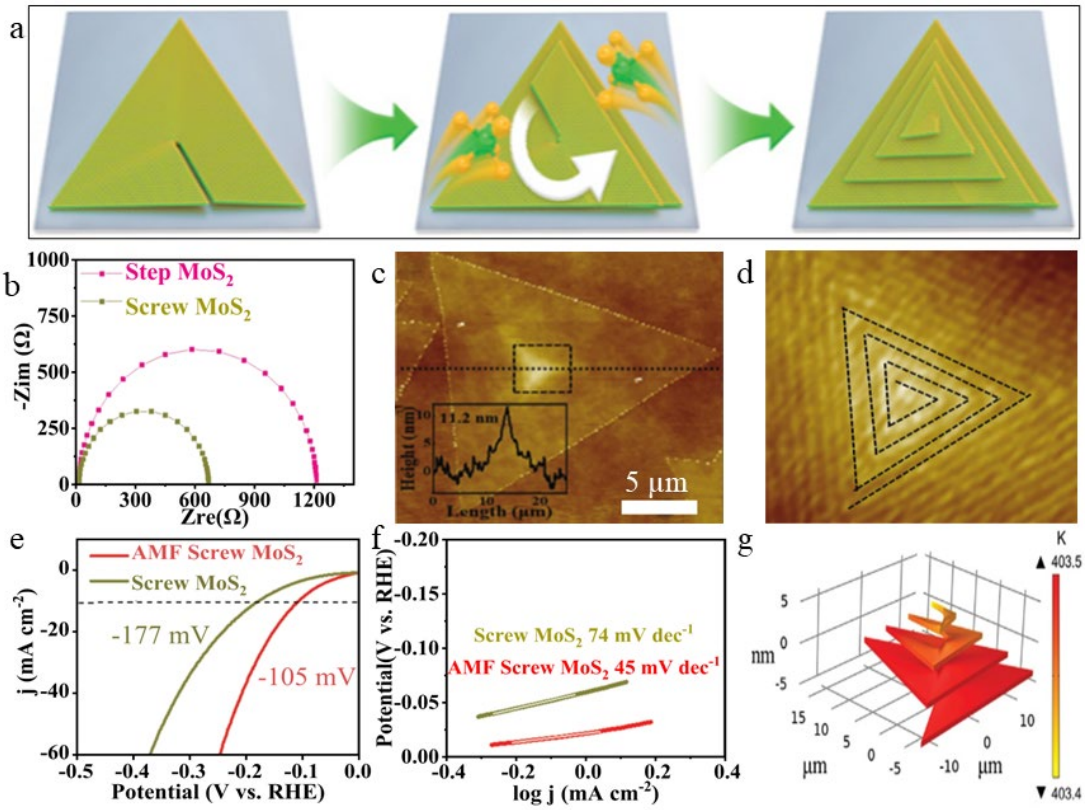

Fig. 3 (a) Synthesis schematic diagram of the screw pyramid MoS_2. (b) EIS Nyquist plots of the screw pyramid and step pyramid MoS_2. (c) AFM image of the screw pyramid MoS_2. (d) The amplified AFM image of center region for the screw pyramid MoS_2. (e) HER polarization curves and (f) EIS Nyquist plots of the screw pyramid and step pyramid MoS_2. (g) Simulated temperature field of the screw pyramid MoS_2. Reprinted with permission from Ref. 67. Copyright © 2022, Wiley-VCH GmbH.

In general, there are a large number of generated bubbles during HER and OER procedures, which attach to the electrode surface [65]. The increase in resistance of the charge transfer from the catalyst surface to the electrolyte interface results in increasing the reaction barrier [66]. The bubbles also cover the active area of the reaction, hindering the combination of the reaction intermediate and the charge at the active sites, leading to the charge transfer rate greater than the consumption rate. An electric double layer is formed, which negatively impacts mass transfer. Methods for regulating the catalyst itself are insufficient to solve the above problem. Therefore, the additional factors need to be introduced to aid in the bubble removal process.

One such solution is the application of a magnetic field. It can exert a Lorentz force on moving the charges, creating a solution convection that facilitates the elimination of the bubbles from the catalyst surface and regulates mass transfer. The application of a magnetic field generates a solution convection that accelerates the transport of paramagnetic oxygen, resulting in improving the OER performances [43]. The overpotential of NiFe LDH could reach as minimal as 207 mV@10 $mA \cdot cm^{-2}$, when the applied magnetic field strength was 200 mT.

3.1.2. The impact of magnetocaloric effect on electrocatalysis

The reaction barrier and mass transfer processes of HER and OER are sensitive to the temperature. Previous studies have mainly employed the way of the overall heating for the catalyst to enhance their performance. However, this method is not energy efficient and can easily lead to overheating, damaging the catalyst and shortening its lifespan. In contrast, the local heating of the catalyst through the magnetocaloric effect can reduce the energy consumption and mitigate damage to the catalyst. Eddy current is a magnetic field effect that generates continuous local heating in an alternating magnetic field. However, the multi-layer structure of 2D layered materials hinders the application of the eddy current effect in practical electrocatalysis. The reason is that the inherent interlayer barrier reduces electrons transfer efficiency, inhibiting the generation of eddy currents and resulting in low magnetic heating efficiency. To address this issue, ultrathin spiral pyramid MoS_2 with nanoscale thickness was prepared (Fig. 3c and d) [67]. In Fig. 3a, based on the screw dislocation, the atoms accumulate on the side of the step and grow spirally along the vertical direction, forming a spiral pyramid structure. Electrons can be directly transported along the helical orbitals of the helical pyramid MoS_2, leading to a higher electron transport efficiency (Fig. 3b) and a better eddy current heating effect compared to the layered MoS_2. Under an alternating magnetic field, the local temperature of the spiral pyramid MoS_2 can reach 400 K (Fig. 3g), while the macroscopic temperature only increases by 1.6 °C. The HER overpotential is 105 mV@10 $mA \cdot cm^{-2}$ (Fig. 3e), and the Tafel slope is 45 $mV \cdot dec^{-1}$ (Fig. 3f). The use of a special structure to enhance the magnetic field-assisted electrocatalytic effect is a promising avenue for the further exploration.

3.1.3 The impact of the spin of electrons on electrocatalysis

Tuning the states of spin have been proved to be an effective method for optimizing the performances of electrocatalytic reaction barriers. Among the various ways of adjusting the spin states, applying a magnetic field is a simpler, more universally applicable method compared to adjusting the lattice plane, doping with heteroatoms, and modifying material size. The spin states of transition metal electrons in 2D CoNi@carbon nanosheets was flexibly regulated by a magnetic field [68]. The OER performances was enhanced by a magnetic field. By exerting a magnetic field, the electron spin polarization is induced and the electron arrangement of the outer orbitals is optimized to facilitate the better adsorption of O_2 intermediates. The overpotential of CoNi@carbon nanosheets reduces by 14 mV@10 $mA \cdot cm^{-2}$, and the Tafel slope decreases by 22.41 $mV \cdot dec^{-1}$, under the action of a 360 mT magnetic field. Additionally, the decrease of resistance

associated with the local magnetic field also contributes to the remarkable OER performances.

3. 1. 4. The impact of magnetoresistance effect on electrocatalysis

The magnetoresistance effect is the extraordinary phenomenon characterized by the changes in resistance of a material in response to a magnetic field. And the resistance can hinder the HER and OER performances. Thereby, the better electrocatalytic performances could be achieved by modulating the resistance through a magnetic field. An improved CVD method was designed to convert non-magnetic MoS_2 into the ferromagnetic bowl-like MoS_2 sheets [69]. The asymmetry of the upper and lower spin bands created by S vacancies is the reason why the MoS_2 sheets exhibit magnetism. The magnetic field facilitates electrons transfer from the glassy carbon electrode to the active sites of the ferromagnetic bowl-like MoS_2 sheets, enhancing the HER performances. The current density of the bowl-like MoS_2 sheets under the magnetic field is doubled at a constant overpotential of -150 mV, compared without magnetic field. Identically, the transfer resistance between the NiFe LDH/Co_3O_4 heterojunction and magnetic NF carrier was also reduced under a magnetic field [70]. That's the reason why the OER overpotential of NiFe LDH/Co_3O_4 is 25 mV@50 mA·cm^{-2} at a 10 000 G magnetic field.

3.2 The impact of light on electrocatalysis

2D materials possess the distinctive structures and excellent physicochemical properties, making them widely applied in both photocatalysis and electrocatalysis. It has been demonstrated that light can be introduced into the electrocatalytic system as energy to reduce the activation energy [71], greatly improving the energy usage efficiency and enhancing the HER and OER performances. In the joint system of light and electrocatalysis, light has a substantial influence on generating the photogenerated carriers in the photosensitive material and heating up the entire electrocatalytic system via the photothermal effects. Consequently, the HER and OER performances are positively impacted.

3.2.1. The impact of increasing carrier density on electrocatalysis

Photosensitive materials interact with light to produce the high-energy carriers, commonly known as hot carriers. Hot carriers can easily overcome the reaction barriers and transport resistance, thereby improving the electrocatalytic activity. In metal/semiconductor composite materials, noble metal nanoparticles are used to excite the hot electrons via localized surface plasmon resonance (LSPR) effect, enhancing the electrocatalytic activity of the composite materials. For the composites composed of Ag nanoparticles and $Ni(OH)_2$ nanosheets [71], the composite structure increases the hot electrons generated by light irradiation, which reduce activation energy and improve the intrinsic OER activity of Ag/$Ni(OH)_2$. Similarly, gold nanoparticles were embedded into Pt nanosheets [72], which enhanced the HER properties (the overpotential with light is 19 mV@10 mV cm^{-2}, which is 4 times lower than that with darkness). Furthermore, it was found that the effect of light-assisted HER could be improved by reducing the distance of the hot electrons transfer from the nanoparticles to the active sites [73]. The defects at the edges and

basal surfaces of MoS_2 nanosheets are regarded as the active sites of MoS_2. The best HER performances of Au/MoS_2 under light is observed, when Au nanocrystals are grown at these locations. In addition to LSPR effect, surface plasmon polaritons (SPP) effect also enhances the electrocatalytic activity. The photon energy required for SPP is relatively low, and the metal's distance from the active site has little effect on the electrocatalytic activity [74]. In Fig. 4a and b, Au grating/MXene composite were prepared through the deposition of $Ti_3C_2T_X$ nanosheets on Au gratings [75]. The visible-near-infrared light causes SPP effect of the Au grating, which leads to sub-diffractive focusing of light and increases the hot electron density. The hot electrons generated by the plasma and the photothermal effect of the plasma cause an advancement in the HER dynamics. The overpotential is -49 mV@10 mA·cm^{-2} under 850 nm light illumination (Fig. 4c). Moreover, SPP effect and LSP effect could be combined to synergistically enhance HER activity [76]. In Fig. 4d and e, Au nanoparticles (AuNPs) are firstly loaded on TiB_2 nanosheets and then deposited on Au grating to form Au grating/TiB_2@AuNPs. Both effects are activated simultaneously to increase the absorbable light range and to synergistically enhance the electrocatalytic activity of TiB_2 flakes in any pH electrolytes. Under the conditions of pH<7 and sunlight simulation, the HER overpotential is -100 mV@10 mA·cm^{-2} (Fig. 4f).

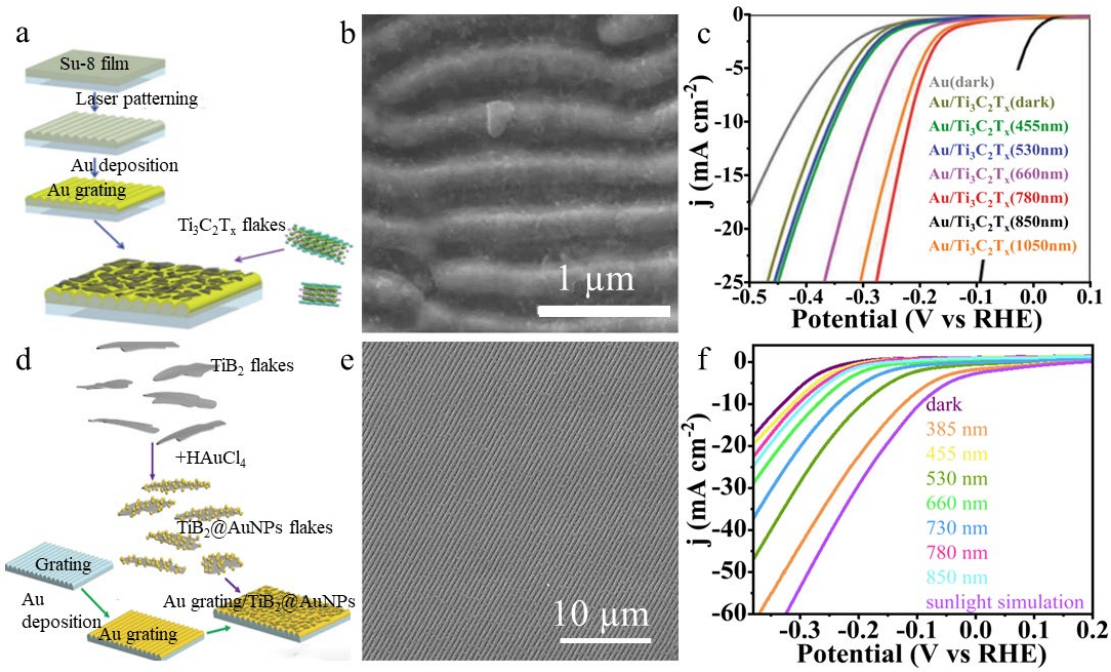

Fig. 4 (a) Schematic representation of the synthesis method of the Au grating/MXene. (b) SEM image of the Au grating/MXene. (c) LSV curves conducted without light and with varying wavelengths of light. Reprinted with permission from Ref. 75. Copyright © 2021, Royal Society of Chemistry. (d) Schematic representation of the synthesis method of Au gating/TiB_2@AuNPs. (e) SEM image of the Au gating/TiB_2@AuNPs. (f) LSV curves of Au grating/TiB_2@AuNPs without light and with varying wavelengths of light. Reprinted with permission from Ref. 76. Copyright © 2023, Elsevier.

However, the plasmon effects require the precious metal materials, limiting its large-scale production. Hence, it is important to develop non-noble metal nanoparticles with a strong LSPR effect. WO_3 nanosheets with oxygen vacancies

possess a strong LSPR effect [77], achieving the HER overpotential of -52 mV@10 $mA \cdot cm^{-2}$ and the Tafel slope of 37 $mV \cdot dec^{-1}$ under the visible-NIR light irradiation. The WO_3 nanosheets with oxygen vacancies could be fabricated by doping P element [78]. And P-N WO_3 homojunctions induced by doping P element facilitate the migration of electron-hole pairs. Additionally, MXene is used to restrain the complexation of the electron-hole pairs, enhancing the light-assisted electrocatalytic HER performances of MXene@P doped WO_3 (the HER overpotential is -44 mV@10 mV cm^{-2}, and the Tafel slope is 41 $mV \cdot dec^{-1}$).

The recombination of carriers during photo-generated carrier transport poses a challenge for improving the photo-assisted electrocatalytic effect. The unique structure of 2D materials gives rise to many special properties. 2D materials with ultra-thin structures, such as Mxene, can reduce the likelihood of the recombination of the electron-hole pairs during transmission. To take advantage of Mxene's good conductivity and ability to capture vacancies, P-TiO_2@Ti_3C_2 composites were fabricated [79]. P-TiO_2@Ti_3C_2 composites is formed by in-situ growth of phosphorus-doped TiO_2 nanocrystals on the surface of 2D MXene (Fig. 5a). The oxygen vacancies caused by MXene and phosphorus doping restrain the recombination of photogenerated carriers, promoting the HER kinetics. In alkaline environment, the overpotential of P-TiO_2@Ti_3C_2 with the assistance of the visible-near infrared is -97 mV@10 $mA \cdot cm^{-2}$ (Fig. 5b), the Tafel slope is 48.4 $mV \cdot dec^{-1}$. And the P-TiO_2@Ti_3C_2 exhibits a remarkable long-term stability, surpassing 50 hours of sustained usage. Furthermore, the construction of a heterojunction can further enhance the HER activity by inhibiting the recombination of photo-generated carriers and promoting charge transfer. For example, atomically thin MoS_2/WS_2 heterojunction was applied to enhance the HER ability of P-type semiconductor WSe_2 [80]. The in situ microscopic photocurrent mapping technique provides a visual insight into the enhanced HER performances induced by the heterojunction (Fig. 5f). The fabricated device with the photolithographic aperture (Fig. 5g) selectively exposes MoS_2 and MoS_2/WS_2 heterojunctions. The photocurrent of MoS_2/WS_2 heterojunction is about 10 times that of MoS_2 (Fig. 5h). Under the simulated sunlight irradiation, the HER overpotential of MoS_2/WS_2 is -0.04 ± 0.05 V@1 $mA \cdot cm^{-2}$. Likewise, N, S-doped graphene quantum dots (GQDs) were combined with graphene to form a van der Waals heterojunction (VDWH) in a study [81]. Under simulated sunlight illumination, the N, S doped GQD/graphene exhibits significantly improved OER and HER performances, with a respective enhancement of 1.75 times and 2.39 times compared to the performances observed in darkness. In a different study, the combination of cobalt porphyrin (CoP) and MoS_2 to form a single atom molecular catalyst CoP/MoS_2 was achieved through electrostatic assembly [82]. CoP acts as a photosensitive material and prevents the aggregation of MoS_2. And the MoS_2 as both 1T and 2H phases, which can improve the conductivity and the intrinsic electrocatalytic activity. Under the sunlight illumination, the overpotential of CoP/MoS_2 is 1.575 V vs. RHE for the overall water decomposition in 0.1 M KOH.

From the aforementioned studies, it is evident that most catalysts employed in

the photo-assisted electrocatalysis are composite materials because only a small group of materials display satisfactory photoelectric effect and electrocatalytic capacity. CoCr LDH nanosheets with rich wrinkles synthesized by hydrothermal method are one of a small group of materials (Fig. 5c) [83]. The Fermi level (E_f) of CoCr LDH is situated between the chemical potential of the OER and the conduction band (E_c) as demonstrated in Fig. 5e, which thermodynamically stimulates the reaction. Furthermore, the Cr element enhances the light absorption ability of CoCr LDH nanosheets. Under the sunlight illumination, the OER overpotential of CoCr LDH decreases by 28 mV@100 mA·cm^{-2} in 1.0 M KOH (Fig. 5d). Besides, $PtSe_2$ films with a thickness of three atomic layers fabricated by using CVD also have a good Photo-assisted electrocatalytic effect [84]. The HER overpotential of $PtSe_2$ films is -0.27 V@1 mA·cm^{-2} under the light illumination.

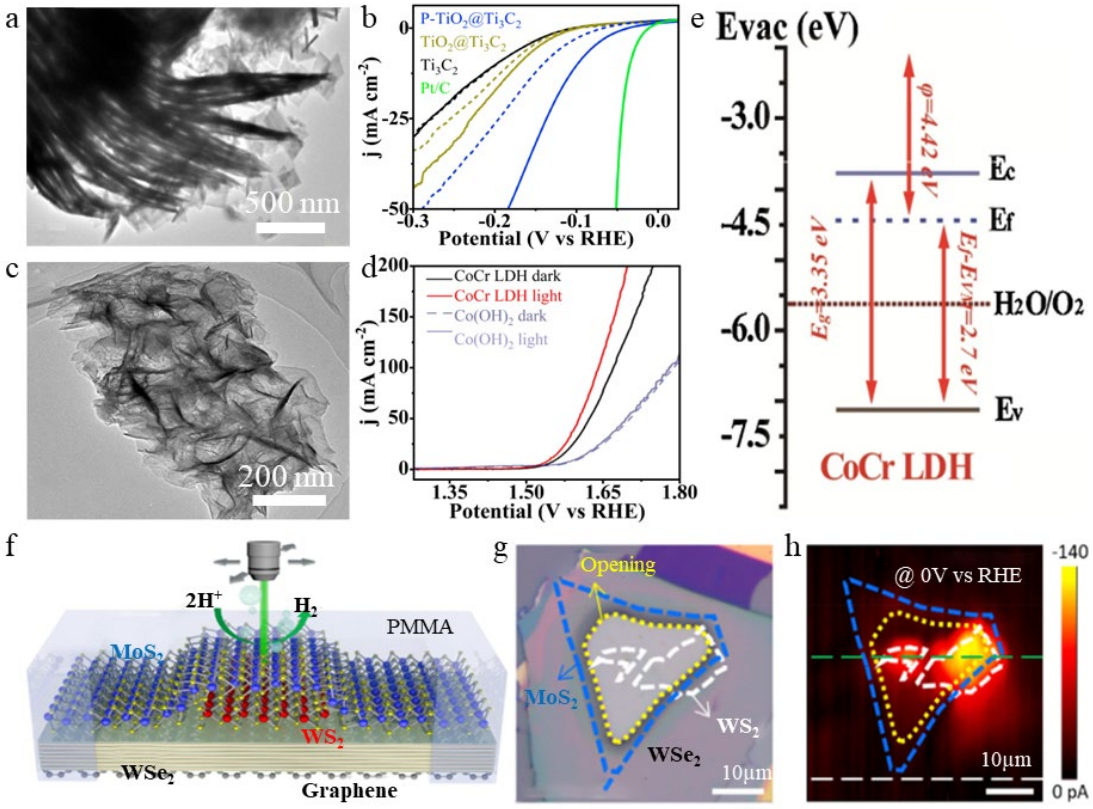

Fig. 5 (a) HRTEM image of P–TiO_2@Ti_3C_2. (b) HER polarization curves of different materials. Reprinted with permission from Ref. 79. Copyright © 2021, Elsevier. (c) TEM image of CoCr LDH nanosheets. (d) IR-compensated LSVs of CoCr LDH nanosheets and $Co(OH)_2$ with (imaginary line) and without the light irradiation (solid line). (e) Energy band diagram of CoCr LDH. Reproduced with permission from Ref. 83. Copyright © 2021, Elsevier. (f) Schematic illustration of the photoelectrochemical measurement. (g) Optical image of the microfabricated device with lithographic opening. (h) Photocurrent mapping image of the device at 0 V vs. RHE. Reproduced with permission from Ref. 80. Copyright © 2019, Elsevier.

3.2.2. The impact of photothermal effect on electrocatalysis

In addition to the excitation of the electron-hole pairs, light can also exert influence on electrocatalysts through photothermal effect. Ni_2P nanoparticles have a good photothermal conversion performance and Quasi-MOF can reduce heat loss [85]. As illustrated in Fig. 6a-c, the Quasi-MOF nanoflakes are loaded on NF and Ni_2P nanoparticles are uniformly dispersed in the nanosheets. Under the sunlight

irradiation, the OER and HER overpotentials of Ni_2P@quasi-Ni-BDC/NF are 246 mV@100 mA·cm^{-2} (Fig. 6d) and -218 mV@100 mA·cm^{-2} (Fig. 6f), respectively, and the OER stability (Fig. 6e) is excellent. On the basis of good photothermal effect, Pt nanoparticles were anchored on Cu_2S/MoS_2 heterostructures to promote electrons transfer [86]. Under the near-infrared irradiation, the overpotential of Cu_2S/MoS_2/Pt is 78 mV@10 mV cm^{-2}, and the Tafel slope is 48 mV·dec^{-1}. Additionally, reduced graphene oxide (RGO) films with a strong photothermal effect were prepared by electrodeposition and thermal reduction [87]. Under the light illumination, the OER overpotential is 215 mV@10 mA·cm^{-2}, and decreases by 93 mV compared to the condition without the light illumination. Additionally, the composite of Ni nanoparticles and RGO can further improve the electrocatalytic performances under the light illumination (the HER and OER overpotentials decrease by -49 and 50 mV@10 mA·cm^{-2}, respectively) [88].

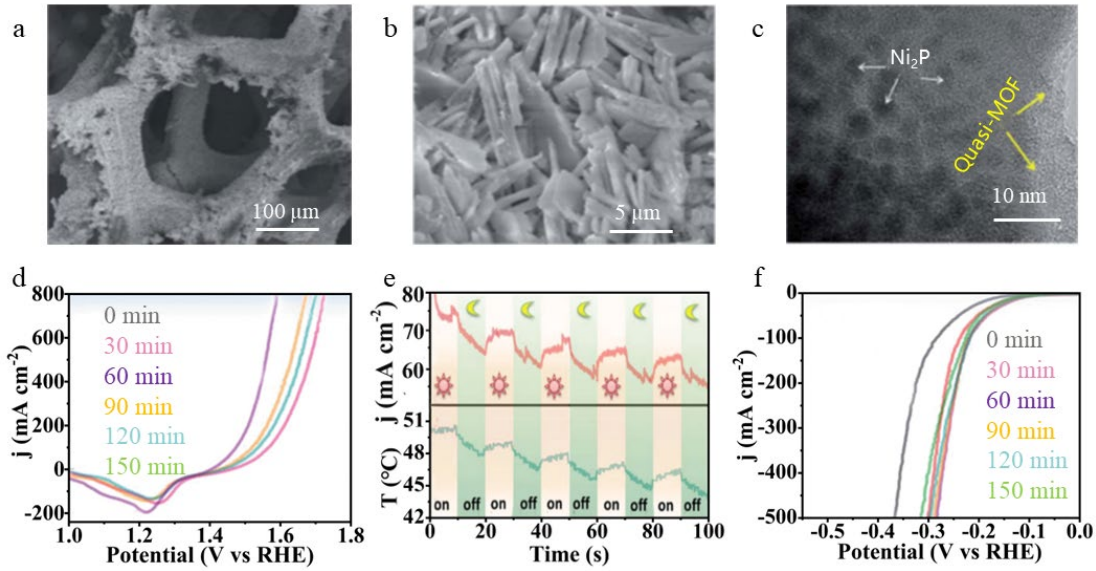

Fig. 6 (a, b) SEM and (c)TEM images of Ni_2P@quasi-Ni-BDC/NF. (d) OER activities of Ni_2P@quasi-Ni-BDC/NF observed at different irradiation times. (e) Catalytic OER current density and temperature responses of Ni_2-P@quasi-Ni-BDC/NF during intermittent light exposure cycles without iR compensation at a constant potential of 1. 523 V vs. RHE. (f) HER activities of Ni_2P@quasi-Ni-BDC/NF observed at different irradiation times. Reproduced with permission from Ref. 85. Copyright © 2021, Royal Society of Chemistry.

3.3 The impact of strain on electrocatalysis

By introducing strain, the electronic structure can be modified and the Gibbs adsorption free energy can be adjusted, leading to a notable improvement in the electrocatalytic activity of the catalyst. That's a commonly used method [89,90]. In accordance with the d-band theory, the strength of adsorption is directly proportional to the proximity of the d-band center to the Fermi level. Conversely, the farther away the d-band center is from the Fermi level, the weaker the adsorption [91]. Strain can regulate the d-band center position and d-band width, so it normally is applied to make the adsorption free energy of electrocatalyst close to 0, resulting in the optimal catalytic performances. When the HER performance was at its best, the intrinsic defect type and tensile strain strength of the electrocatalyst could be calculated by theoretical calculation [92]. The excellent mechanical properties and surface structure

of 2D materials make them ideal for studying strain effects. To achieve real-time visualization of the enhanced HER activity induced by strain, the combination of in-situ electrochemical scanning tunneling microscopy (EC-STM) and current noise analysis (n-EC-STM) was employed [93]. The electrocatalytic active sites at nanoscale are identified through the analysis of relative variations in tunneling current noise observed throughout the HER, showing the enhancement of the strain-induced HER activity of MoO_2 nanosheets at the nanoscale. Moreover, the 2D electrocatalysts have the intrinsic strain, which is one of the reasons for the excellent electrocatalytic performances of the 2D electrocatalysts. Due to the attractive force between 2D films [94], thinner films have greater compressive strain, which can significantly improve the OER and HER activities. Additionally, the absorption of hydrogen on the catalyst surface exerts the stress that counteracts the intrinsically compressive strain, leading to the lattice stretched and influencing the electrocatalytic performances [95].

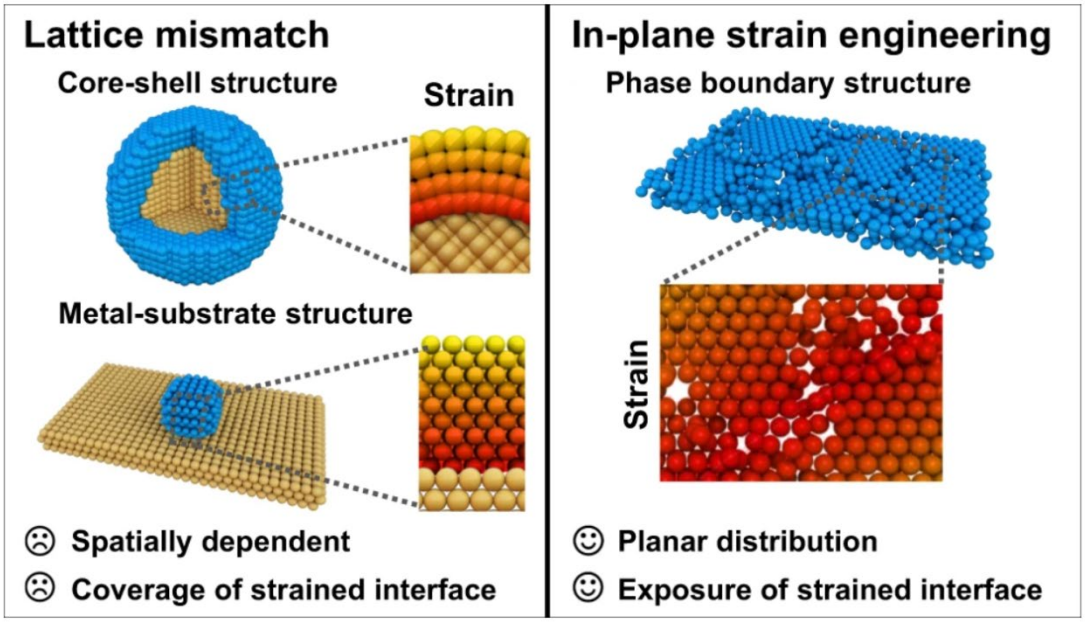

Fig. 7 By establishing the lattice mismatch in core-shell structure or metal-substrate structure, and utilizing in-plane strain engineering through the construction of amorphous-crystalline phase boundaries, strain can be engineered. Reprinted with permission from Ref. 96. Copyright © 2022, Nature Portfolio.

The strain can be induced into 2D materials through forming wrinkles, bends, and other shapes. For instance, curved ultrathin PtPd nanodendrites were successfully created through the introduction of the compressive strain into 2D nanosheets [97]. The compressive strain modifies the regional coordination environment of the active sites in the PtPd nanodendrites, causing the energy density of the d-band center to decrease. Thereby, the ability of absorbing H* of the PtPd nanodendrites is enhanced, and ultimately the HER activity of curved ultrathin PtPd nanodendrites is improved (The overpotential is -10.8 mV@10 $mA \cdot cm^{-2}$). Likewise, curved palladium-iridium (PdIr) bimetallene with an average thickness of 2.1 nm also have the remarkable HER performances [98], with an HER overpotential of -34 mV@10 $mA \cdot cm^{-2}$ in alkaline environment. In another study, α-$Co(OH)_2$

nanoflowers composed of curly nanosheets were synthesized [99], with an OER overpotential of 269 mV@10 mA·cm^{-2}.

For single atom catalysts, the low loading density and unreliable loading position limit the electrochemical activity of the single atom catalysts. However, this issue has been solved. Through the application of electrochemical cyclic voltammetry, a single atom Cobalt array was successfully anchored onto the distorted 1T-MoS_2 nanosheets, resulting in the creation of a single atom catalyst (SA Co-D 1T MoS_2) [100]. The stress induced by the lattice mismatch between Co and 1T-MoS_2, combined with the establishment of Co-S bonds, jointly induce the transformation of 2H MoS_2 into the twisted 1T-MoS_2. The HER overpotential of the SA Co-D 1T MoS_2 catalyst is -42 mV@10 mA·cm^{-2}, and the Tafel slope is 32 mV·dec^{-1}. The SA Co-D 1T MoS_2 catalyst demonstrates the HER performances that are akin to the Pt/C catalyst used in commercial application.

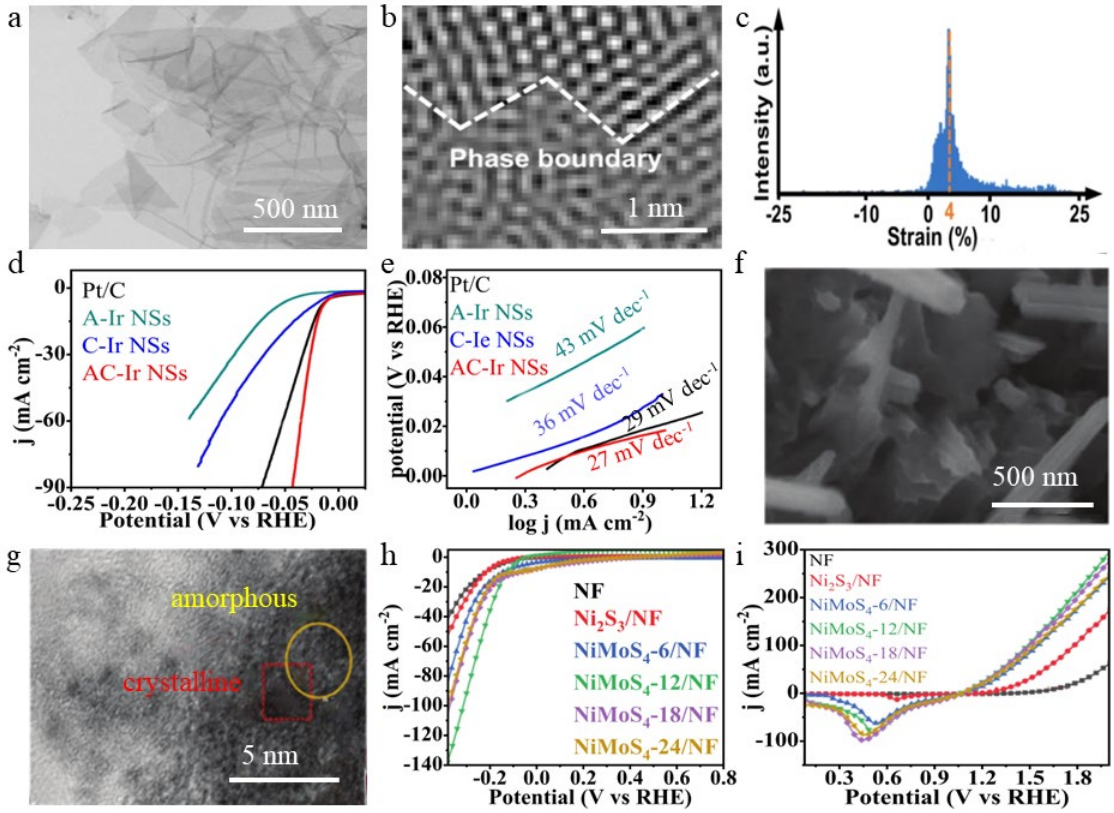

Fig. 8 (a)TEM image of AC-Ir NSs. (b) High-resolution TEM image displaying the amorphous-crystalline boundary within the AC-Ir NSs. (c) Histogram representing the distribution of strain within the nanosheets. (d) Polarization curves and (e) the corresponding Tafel plots of Pt/C, amorphous Ir nanosheets (A-Ir NSs), crystalline Ir nanosheets (C-Ir NSs) and AC-Ir NSs. Reprinted with permission from Ref. 96. Copyright © 2023, Nature Portfolio. (f) SEM image of $NiMoS_4$-12/NF. (g) TEM image of flake $NiMoS_4$-12. IR-compensation LSV curves of NF, Ni_3S_2/NF, $NiMoS_4$-x/NF (x = 6, 12, 18, and 24) for HER(h) and (i) that for OER, x indicates the holding time of the hydrothermal method. Reprinted with permission from Ref. 105. Copyright © 2022, Royal Society of Chemistry.

In addition to altering the morphology of nanosheets, it is also a broad method to introduce the strain by combining two materials with huge lattice differences. Ni_2P nanospheres were grown on the defective MXene to form heterojunctions [101]. The noticeable lattice distortion at the heterojunction interface is a consequence of the lattice disparity [102] between the Ni_2P nanospheres and MXene, ultimately giving

rise to the formation of the Ni_2P hollow spheres. The HER overpotential of the Ni_2P@MXene is -123.6 mV@10 mA·cm^{-2}, and the Tafel slope of 39 mV·dec^{-1} in 0.5 M H_2SO_4 electrolyte. Additionally, the HER performances of the Ni_2P@MXene are also outstanding in electrolytes with neutral pH and alkaline conditions.

The surface strain caused by the lattice mismatch is commonly observed in the core-shell nanostructures [103,104] and metal-substrate interfaces (Fig. 7). But the strain typically decreases with the increasing distance from the interface, and the abovementioned structures limit the exposure of the active region. However, the strain engineering in the nanosheet is completely different. Amorphous-crystalline Ir nanosheets (AC-Ir NSs) (Fig. 8a and b) were created by a salt-assisted annealing approach [96]. A 4% tensile strain is observed in AC-Ir NSs (Fig. 8c), due to the introducing of amorphous-crystalline boundaries in the plane of Ir nanosheets. The HER overpotential of AC-Ir NSs is only -17 mV@10 mA·cm^{-2} (Fig. 8d), and the Tafel slope is 27 mV·dec^{-1} (Fig. 8e). Similarly, Crystalline and amorphous $NiMoS_4$ nanosheets were synthesized on NF via using the hydrothermal method [105]. The material synthesized at a holding time of 12 h has two forms: rod-like and sheet-like (Fig. 8f). In $NiMoS_4$ nanosheets, the interfacial strain occurs at the interface between the crystalline and amorphous states (Fig. 8g), leading to the crystal plane deformation and numerous sulfur vacancies, which improves the intrinsic catalytic activity. The crystalline and amorphous $NiMoS_4$ nanosheets show the excellent overall water decomposition performances and durability, with the HER and OER overpotentials of -119 mV@10 mA·cm^{-2} (Fig. 8h) and 273 mV@10 mA·cm^{-2}(Fig. 8i), respectively.

However, the aforementioned methods of applying lattice strain through material synthesis have certain limitations. In contrast, the method of applying lattice strain through the mechanical means is more easily controlled and simplified. The hydrogen adsorption capacity of nanocrystalline palladium film decreased by 1.1%±0.4% under 2% mechanical tensile strain [106], and the HER activity increased by 5.7%±1.7% under 4.5% mechanical tensile strain.

Strain can have a significant impact on the enhancement of the catalytic performances, but not all 2D materials show improved electrocatalytic activity under the strain, such as phosphorus carbide (PC) [107] and B_7P_2 [108]. Therefore, it is essential to further investigate the impact of the strain on the electrocatalytic performances. Through the density functional theory (DFT) calculations, it was easily obtained that Co^{3+} in the 2D CoOOH can be transformed from a low-spin state to a high-spin state through applying 9 % biaxial strain [109], and the OER performances of the CoOOH is significantly improved. Similarly, the roles of strain in modulating the electrocatalytic activity of Co, N co-decorated graphyne (Co@N_1-GY) nanosheets for overall water splitting were explored by using first-principles [110]. The calculation results revealed that the material achieved the best HER performances under the 0.5% tensile strain, and the minimum OER overpotential was 0.33 V at the bidirectional tensile strain of 3%. And, the structure of single atom catalyst can increase the strain sensitivity [111]. Additionally, the ability to fix metal atoms can be enhanced by bending the single-atom-loaded nanosheets [112]. When the proper compressed and

loaded metal is chosen, the HER electrocatalytic activity and OER overpotential are equivalent to that of Pt. Furthermore, some potential strain-sensitive 2D electrocatalysts have been found through theoretical calculations. The Gibbs free energy of Ni-MoS_2 monolayer is close to 0 eV and the HER performances are the best in the alkaline environment when biaxial strain ranges from 11% to 12%, so a Ni-MoS_2 monolayer is highly responsive to strain [113]. In another study, a graphene-based 2D carbon allotrope with metallic properties was constructed by using the genetic algorithm [114]. By applying to a specific amount of the compressive strain, graphene exhibits superior HER performance to Pt catalyst and has better OER activity. Similarly, it was demonstrated through DFT calculations that the hydrogen adsorption free energy of the corrugated transition metal disulfide monolayer (W-MS_2) was significantly reduced by the compressive strain [115], leading to the excellent HER performances. Furthermore, a new type of 2D MOCN monolayer with the higher HER activity than Pt was discovered via the combination of global minimum structure search and first-principles calculations [116]. The electrocatalytic activity of the monolayer can be further improved by applying the strain. Finally, it was demonstrated that the HER activity of Cr_2O_3 monolayer can be stimulated by the strain [117], via using DFT. The Gibbs free energy of H* adsorption is calculated to be 0.09 eV after strain application.

3.4 The impact of electric field on electrocatalysis

Electric field is a physical field closely related to the electrochemistry. It exists at the composite interface [118] and the catalyst/electrolyte interface [119]. And the purpose of the precise regulation of the electron density can be achieved via exerting the external electric field. Therefore, the influence of the external electric field on electrocatalysis has attracted wide attention. In the coupling system of the electric field and electrochemistry, under an electric field, the HER and OER performances can be optimized by changing the adsorption energy and conductivity, polarizing electrons and generating hot electrons.

3.4.1 The impact of conductivity on electrocatalysis

The electric field can enhance the electrocatalyst activity by decreasing the conductivity of the electrocatalyst and contact resistance between the electrode and electrocatalyst. By applying a solid-state ion-gated technology instead of SiO_2/Si to adjusting the Gibbs free energy and enhancing the conductivity of the electrocatalyst [120], the HER performances of MoS_2 can be improved. The enhancement of the HER performances caused by the improved conductivity can be explained. In electrochemistry, in order to enable the Fermi level to equal the redox potential of a specific reaction, sufficient energy needs to be applied to overcome the required thermodynamic potential (overpotential) (Fig. 9a and b). The electric field as the energy makes the Fermi level between the conduction band and H_3O^+/H_2 potential, resulting in the thermodynamic activation for the reaction. In a separate study, it was demonstrated for the first time that the HER performances can be affected by regulating the Fermi level of 2H-MoS_2 through an electric field [121]. With the increase in gate voltage from 1 V to 2 V, the MoS_2 experiences the semiconductor-metal transition and the Fermi level position of MoS_2 undergoes a transition from −4.3 eV

to −3.93 eV (Fig. 9d-f). At the interface of the semiconductor and electrolyte, electrons must overcome the out-of-plane band gap (2. 3 eV). When the gate voltage increases to 3V, the Debye screen length decreases to 1 nm, causing the electrons to be confined in a layer of MoS_2, with only the requirement of overcoming the in-plane band gap (1.3 eV). Moreover, an electric field causes the accumulation of the electrons in MoS_2, making the Fermi level of 2H-MoS_2 move to the location between the conduction band and the H_3O^+/H_2 potential. The electrons transfer barrier from the electrocatalyst to the reactant reduces. As a result, the HER performances have been significantly increased. The HER overpotential of 2H-MoS_2 is 74 mV@10 mA·cm^{-2} (Fig. 9c) at 3 V gate voltage.

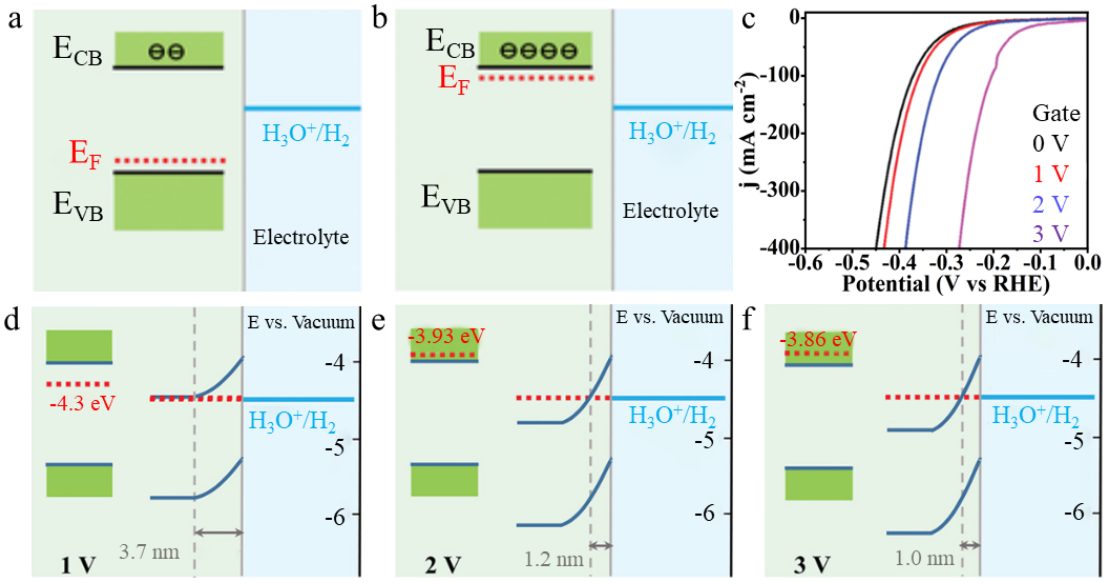

Fig. 9 (a, b) Diagram illustrating the energy band structure. (c) The HER performances of 2H-MoS_2 under varying gate voltages. (d–f) Diagram illustrating the energy band structure. 2H-MoS_2 under the gate voltages of 1, 2, and 3 V, respectively. Reprinted with permission from Ref. 121. Copyright © 2022, Wiley-VCH GmbH.

3.4.2 Changing the adsorption energy

Achieving an excellent HER performance requires a balance between adsorption and desorption of adsorbed intermediates. with a Gibbs free energy of hydrogen adsorption (ΔG_H) of 0 being ideal. While regulating the morphologies, structures, composition, and defects of 2D materials can lead to achieving ΔG_H close to 0, the methods do not allow for precise regulation. Fortunately, the electric field have a significant impact on ΔG_H and can be adjusted to achieve the precise regulation. Additionally, the activity of 2D electrocatalyst is easily regulated by an external electric field because of the weak electrostatic shielding effect. For the monolayer MoS_2 [122], a positive gate voltage increases the charge of the active sites, thereby Significantly strengthening the Mo-H bond and enhancing the HER activity. An electric field led to a reduction in the HER overpotential by 140 mV@50 mA·cm^{-2}, compared to the situation without an electric field.

Both the electric field and the heterojunction can enhance electrons transfer, and the strengthening effect of the two can be superimposed. So, an in-plane and inter-plane double heterojunction structure of ReS_2/WS_2 was constructed (Fig. 10a)

[123], to strengthen the HER performances under an electric field. The vibration peaks of ReS_2 and WS_2 appear at the base surface (Fig. 10d), indicating the vertical stacking of ReS_2 and WS_2. And the curve at the edge is consistent with the double-layer WS_2, indicating that both ReS_2 and WS_2 exist in a plane. The heterojunction is triangular (Fig. 10b) and the atomic arrangement of vertically stacked regions of ReS_2 and WS_2 is significantly different from that of the bilayer WS_2 region (Fig. 10c). The double heterojunction structure induces directional electron transfer from WS_2 to ReS_2. These are the evidence to prove the existence of double heterojunction structure. The structure leads to improve the in-plane and inter-plane electrons transport, redistribute charge at the interface, and optimize adsorption and desorption of H*. The double heterojunction structure induces the directional electrons transfer from WS_2 to ReS_2, resulting in improving the in-plane and inter-plane electrons transport, redistributing charge at the interface, and adjusting the adsorption and desorption of H*. An external electric field is applied to promote the electrons transport, achieving the precise regulation of the HER activity. The experimental installation of the electric field-assisted electrocatalytic HER (Fig. 10e) is seen as a coupled field effect transistor and an electrocatalytic cell sharing a ReS_2/WS_2 nanosheet. The entire device is coated with a layer of polymethyl methacrylate resist to selectively expose the region for the electrocatalytic reaction. The three-electrode microreactor is fabricated on the SiO_2/Si substrate to construct a metal-oxide-semiconductor heterostructure that provides an electric field during the electrocatalytic process. An optimal HER performance is achieved at a 6 V gate voltage, with an overpotential of the double heterojunction catalyst of -49 mV@10 $mAcm^{-2}$ (Fig. 10f) and a Tafel slope of 35 $mV \cdot dec^{-1}$ (Fig. 10g).

Take a van der Waals heterojunction of cobalt phthalocyanine (CoPc) and MoS_2 as an example, the charge transfer at the heterojunction interface was studied under an external electric field [124]. The energy level distribution of the CoPc molecule and MoS_2 is adjusted by the vertical electric field, which reduces the potential barrier of the charge transfer from CoPc molecule to MoS_2 and allows electrons to be unidirectionally injected from CoPc into MoS_2 nanosheets. The excess charge is then further distributed to the Mo atom near the S vacancy in MoS_2, resulting in a linear increase of the intrinsic activity. The charge density around the Mo atom is precisely controlled by adjusting the electric field. The van der Waals heterojunction interface under the action of this electric field is called the van der Waals charge channel. When the back gate voltage reaches 2 V, the carrier density on the van der Waals charge channel increases by 1.48×1012 cm^{-2}, the HER overpotential is -63 mV@10 $mA \cdot cm^{-2}$, and the Tafel slope decreases linearly under the electric field.

The electrocatalytic transistor structure is commonly used to study the impact mechanisms of the electric field on the electrocatalytic HER and OER [125,126]. Furthermore, a similar mechanism was observed in the electrocatalytic mechanism of 2D materials [119]. During the electrocatalytic HER of the n-type semiconductor MoS_2 film, the positive charge in the electrolyte converged to the electrode surface acting as the gate, and the active site on the film acted as the drain. The conductive substrate acted as the source, and the inert substrate acted as an insulator, isolating

electrons. The electric field applied by the gate accelerated the electrons in the process of transferring from the source to the gate, thus improving the surface conductivity. This mechanism also explains the excellent catalytic performances of 2D materials.

3.4.3 The impact of polarizing electrons on electrocatalysis

Additionally, the electric field can optimize the electrocatalytic activity by polarizing electrons. The mechanism of polarizing the electrons was found in the study of HER performance of single atom catalysts under electric field [127]. The Pt single-atom catalyst on the n-type MoS_2 exhibits the HER overpotential of 20 mV@10 $mA \cdot cm^{-2}$ and a Tafel slope of 51 $mV \cdot dec^{-1}$ under a gate voltage of +40 V. The Co single-atom catalyst on p-type WSe_2 displays the OER overpotential of 139 mV@10 $mAcm^{-2}$ and a Tafel slope of 64 $mV \cdot dec^{-1}$ under a gate voltage of -40 V. The DFT results reveal that the external vertically electric field accurately regulates the charge distribution of the active sites of the single-atom catalyst, polarizes the outer orbital metal/intermediate, changes reaction path, reduces energy barriers, and does not regulate the carrier density. In a different study, the feasibility of using the ferroelectric materials as switch composites on 2D catalysts to control the HER activity was demonstrated via the DFT [128]. The composite material that transition metal Co is embedded in the nitrogen-doped graphene and is loaded on the ferroelectric material In_2Se_3 exhibits the optimal electrocatalytic performances when the polarization direction is downward. The polarization direction changed from upward to downward induces the redistribution of electrons, transfers the electrons to In_2Se_3, decreases the electrons density of the active sites, reduces the Co-H bond energy, and increases the HER activity.

3.4.4 Hot electrons

It is revealed in section 3. 2. 2 that light has the ability to stimulate the production of hot electrons, which participate in the electrocatalytic reaction. Similarly, an electric field can also excite hot electrons. For the Pt/Si metal-semiconductor nanofilm [129], the acceleration of electrocatalytic HER was promoted because of the generated hot electrons under an electric field. In the electrocatalytic process, the hot electrons are produced, which move spontaneously through the metal-semiconductor heterojunction to take part in the HER at the active sites on the surface of the Pt nanofilm. The usage of an electric field leads to an 8-fold increase in cathode current and causes the overpotential to move forward by 160 mV. However, when the thickness of the Pt film increases to a certain threshold, the effect becomes negligible. Thereby, this technique particularly is suitable for 2D materials. In comparison to the light field, the approach that the hot electrons are generated by an electric field provides better controllability and is more conducive to studying the hot electron injection process.

3.5 The effects of the other physical fields on electrocatalysis

In addition to the aforementioned magnetic field, light, strain, and electric field, there are two additional factors that can affect the electrocatalytic activity: temperature field and ultrasonic wave. The effects of a temperature field on electrons transfer efficiency of the electrolyte and catalyst are significant and can

activate the active base surface of 2D materials, enhancing their catalytic activity. Most studies increase the temperature by using magnetic [69], light [85-88], and electric [129], as it is easier to control. For instance, the HER overpotential of MoS_2 monolayer was improved to 90 mV@10mA·cm^{-2}, when the temperature was raised to 60°C through controlled laser heat generation [130]. Ultrasound is frequently used in the material synthesis stage, but there have been few studies on the application in the electrocatalytic process, most of which remain at a macro level. The OER performances of Au nanoparticles supported on MoS_2 nanosheets can be enhanced by ultrasonic vibration [131]. Because the ultrasonic wave deforms the nanosheets producing a piezoelectric effect that increases the conductivity of Au nanoparticles and thereby improvs the OER performances.

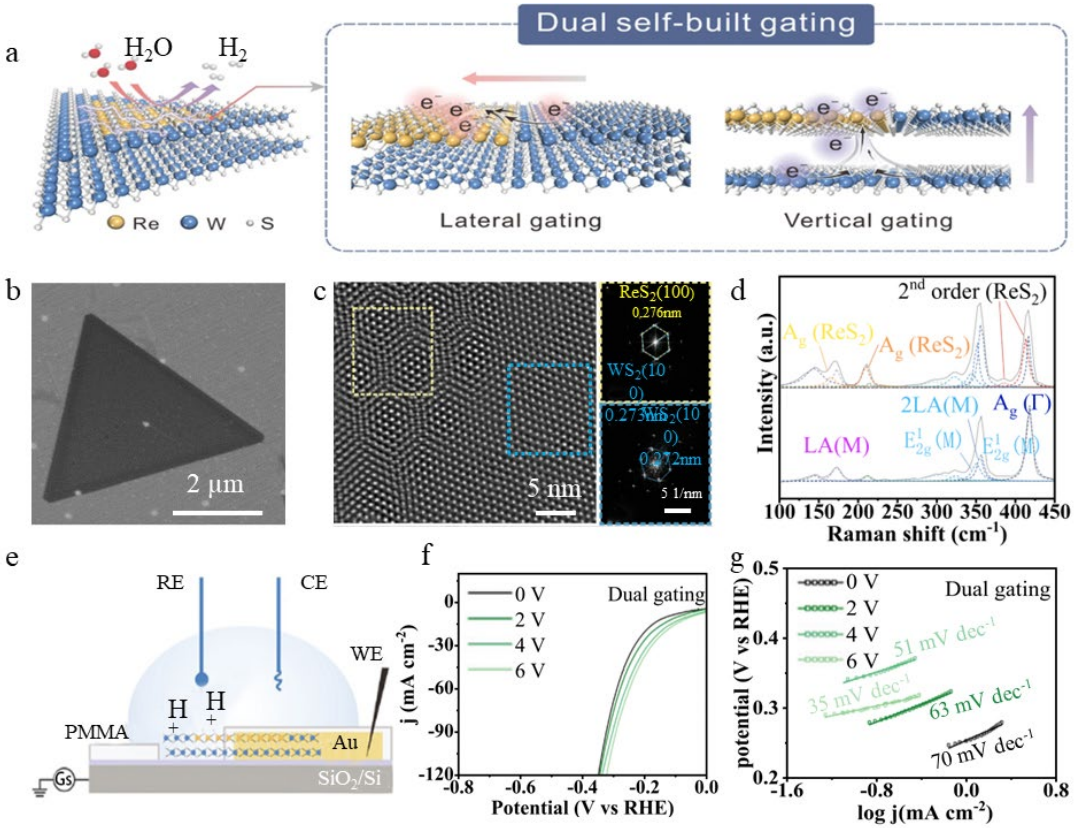

Fig. 10 (a) Illustration of hybridized lateral and vertical ReS_2–WS_2/WS_2 (HLV) heterostructure that enhances the HER kinetics. (b) TEM and (c) STEM image of the HLV heterostructure, with the smaller figures on the left displaying the FFT of the yellow and blue regions in (c), revealing the diffraction spots of ReS_2/WS_2 and WS_2, respectively. (d) Raman spectra obtained at the edge and the basal plane of the HLV heterostructure, corresponding to outer bilayer WS_2 (the lower part) and internally vertical stacked ReS_2/WS_2 Heterostructure (the upper part), respectively. (e) Schematic illustrations depicting the micro-electrochemical device used to measure the HER performances of the HLV heterostructure. (f) HER polarization curves and (g) Tafel slopes of HLV heterostructure at various gate voltages. Reprinted with permission from Ref. 123. Copyright © 2022, Wiley-VCH GmbH.

Furthermore, it should be noted that these physical fields can coexist. A heterojunction of single-layer WS_2 and MoS_2 was created, and it was then formed into nanoscrolls [132]. The unique heterojunction results in the HER performances under the strain and light interaction comparable to the HER performances of noble metal catalysts. Similarly, Non-uniform strain was induced through the creation of a wrinkled structure on a single-layer WS_2 film. And the influence of light and strain

coupling on electrocatalytic HER is examined [133]. The high strain region is located at the wrinkle peak, while the low strain region is situated at the wrinkle valley. The strain gradient between the two regions alters the energy band structure and generates an electric field based on the piezoelectric effect, facilitating the separation of hole-electron pairs. Additionally, the structure enhances the contact surface between the WS_2 film and the substrate, thereby decreasing the interface scattering effect and increasing carrier mobility. Compared to the planar structure, the Tafel slope of the wrinkled WS_2 for the HER decreases from 133 $mV \cdot dec^{-1}$ to 59 $mV \cdot dec^{-1}$, and the current density at -0.5 V increases from 3.5 $mA \cdot cm^{-2}$ to 104.7 $mA \cdot cm^{-2}$. Moreover, the HER and OER overpotentials of the reduced graphene oxide on nickel foam were observed to be -157 and 324 mV@10 $mA \cdot cm^{-2}$, respectively [134], under the magnetic and light fields. The combined effect of multi-fields is often more substantial than that of a single field, highlighting the need for further research into the synergistic effect of multiple fields on electrocatalysis.

3.6 Effect of the external physical fields on hybrid materials based on 2D materials

Zero-dimensional (0D), one-dimensional (1D), and 2D materials possess varying physicochemical properties. A reasonable combination of these materials can improve the effect of the external physical field-assisted electrocatalytic HER and OER. The inability of 2D materials to meet all the requirements of electrocatalyst for field-assisted electrocatalytic systems, so they require compounding with the other low-dimensional materials to meet the required specifications. The composite materials are mentioned in the above magnetic field (3.1.4), light field (3.2), strain (3.3), electric field (3.4.3) and other physical fields (3.5), especially in photo-assisted electrocatalytic systems. The electrocatalytic activity of SnS_2/NiO heterojunction under visible light irradiation have a great enhancement [135]. For this hybrid system, the holes accumulate in the NiO particles, promoting the formation of Ni^{3+} and improving the intrinsic activity of OER, resulting in the overpotential of 310 mV@10 mV cm^{-2}. Additionally, a lower OER overpotential and Tafel slope were observed in the BP quantum dots/MoS_2 heterojunction [136], under the light illumination. Similarly, Zn-$AgIn_5S_8$ quantum dots (ZAIS QDs) [137], a light-absorbing material, were embedded into NiFe LDH nanosheets by a hydrothermal method. The structure enhances the ability to decompose water, resulting in a -151 mV@10 mV cm^{-2} overpotential for HER under the dark conditions. However, under the light, the overpotential decreases to -22 mV@10 mV cm^{-2}. Furthermore, under the light conditions, the OER overpotential is 220 mV@10 mV cm^{-2}, and the intrinsic activity is twice as that under the dark conditions.

1D nanomaterials possess an impressive ability for the directional charge transfer, making them ideal for enhancing the conductivity of the composite materials. 1D graphene oxide nanoribbons were incorporated onto a 2D WS_2/g-C_3N_4 heterojunction [138]. The combination leverages the strong photosensitivity and conductivity of graphene nanoribbons and WS_2/g-C_3N_4 heterojunction to overcome the issue of photogenerated carrier recombination, resulting in the highly active catalytic sites. These characteristics enable the composite to exhibit the remarkable HER performances under the light illumination,

with the overpotential of -150 mV@10 mA·cm^{-2}. Moreover, three low-dimensional materials were combined to improve the light-assisted OER performances [139]. The recombination of photogenerated carriers generated by p-n $WO_3/SnSe_2$ heterojunction particles is inhibited, and carrier transfer is promoted by CoFe LDH and carbon nanotubes, which jointly result in greatly enhanced OER activity of CoFe LDH/carbon nanotubes. The OER overpotential under the visible light irradiation is reduced to 224 mV@10 mA·cm^{-2}, and the Tafel slope is 47 mV·dec^{-1}.

Additionally, a special core-shell structure was constructed to introduce the strain and promote the OER activity [103]. By inducing the compressive strain through the construction of an IrO_x atomic layer on the IrCo nanodendrites, the OER activity is enhanced. The IrCo nanodendrites with 2 IrO_x atomic layers and 1.51% compressive strain exhibit the best OER activity with an overpotential of only 247 mV@10 mA·cm^{-2}. Density functional theory (DFT) suggests that the compressive strain significantly regulates the kinetics of the intermediate (HOO*) adsorption, thereby improving the OER activity.

It can be seen that the morphology and size of low-dimensional materials have a significant impact on the improvement of electrocatalytic performance in the external field. Therefore, it is necessary to regulate the microstructure of the catalyst. The effective engineering of heterogeneous organic/inorganic nanocrystals with multiple hybrid composite domains, high, and low active surface sites, and mesoscopic hierarchy architectonics for electrocatalysis applications was recently reported by El-Safty's Group [140–147]. For example, the control synthesis and homogeneous diffusion of several composite particles through self-propelled, particle-in-particle diffusion enabled fabrication of a wide range of heterogeneous organic/inorganic nanocrystals in mesoscopic architectonics. These hybrid materials with specific functional groups have the ability to synergistically enhance catalytic properties, stability, and conductivity, as well as enhance the affinity for oxygen.

4 Summary and outlook

Growing energy demand and severe environmental problems have led to an increased focus on the usage of the hydrogen energy. Therefore, the industry urgently requires an economical and high-efficiency electrocatalyst for water splitting. 2D materials have high surface volume ratio providing the ample active sites for adsorption, and their unique physicochemical properties ensures the rapid electrons transfer, making them potential HER and OER electrocatalysts. Methods such as heteroatom doping, defect engineering, surface functionalization, and composite structure have emerged to improve the electrochemical HER performances of 2D nanosheets, resulting in a major breakthrough in the high electrocatalytic performances. Yet, to create the HER and OER electrocatalysts that surpass the commercial noble metal catalysts, there is a need to introduce an additional design factor to the catalysts, namely the external physical fields. Therefore, this paper aims to summarize the research of the external physical field-assisted synthesis of 2D electrocatalysts and external physical field-assisted electrocatalytic HER and OER. The effects of the physical fields on catalyst synthesis and the basic principles of

different fields to enhance the electrocatalytic performances of 2D materials are preliminarily summarized.

The influence of the physical fields on material synthesis can be summarized as follows: (1) Ultrasound can assist in the exfoliation of 2D layered electrocatalysts and promote the generation of composite materials. (2) The magnetic field can aid in inducing the phase transition in material synthesis. And the magnetocaloric effect heating method can replace the traditional heating method, which is a local heating method with faster heating speed and lower energy consumption. (3) Microwave heating can heat materials faster and more evenly during synthesis.

The mechanisms of the external field-enhanced electrocatalysis can be preliminarily summarized as follows: (1) The temperature field can effectively reduce the charge transfer impedance, activate inert surfaces, and accelerate the release of bubbles on the catalyst surface. Since the other physical fields can also produce thermal effects that assist catalytic reactions, the temperature field generally enhances both the HER and OER activity, along with other physical fields such as magnetic field, light, and electric field. (2) The applied electric field is particularly suitable for 2D electrocatalysts with weak shielding effects. The electric field can reversibly control the adsorption energy, polarize electrons, and reduce resistance. Additionally, heterojunction construction allows for the better use of an electric field regulation on carriers. (3) Besides electric field, magnetic field can also promote charge transfer, change the spin states of the electrons at active sites, and regulate the intermediate adsorption. Additionally, the magnetohydrodynamic effect of the magnetic field can regulate the electrolyte composition at the interface and force the bubbles to separate from the electrode surfaces. (4) Photogenerated carriers, generated by the photoelectric effect, can change the electronic structure of active sites, optimize the adsorption energy, and increase the catalytic activity. The unique structures of 2D materials can promote the separation of the photogenerated carriers and charge transfer. (5) Strain can alter the position of d-band center and d-band width, adjusting the adsorption energy. Moreover, strain can adjust the spin states.

Although considerable advances in the field-assisted electrocatalytic HER and OER have been made, these studies are still in their infancy and face numerous challenges. The primary issues include: (1) Imperfect structure of the field-assisted electrocatalytic system. For instance, the gate electrode used in the electric field-assisted electrocatalysis is predominantly SiO_2/Si gate. The capacitance of SiO_2 as the dielectric layer is low, and the carrier density generated by the electric field is inadequate. Replacing it with a material of higher capacitance could enhance the effect of the electric field-assisted HER and OER. (2) The practicability of the field-assisted electrocatalysis. This technology can only be implemented in practical applications when the energy consumption associated with introducing or maintaining the physical fields is significantly lower than the increased electrocatalytic performances by the physical fields. Furthermore, durability is another factor that affects the practical application of this technology. The catalyst will undergo structural reorganization during operation, leading to the attenuation of the strain and affecting the efficacy of the strain-assisted HER and OER. (3) There is

insufficient research on the physical field-assisted electrocatalysis, such as sound field and electric field, and the specific mechanisms of influencing the HER and OER performances are not yet fully developed. Furthermore, there are few studies on multi-field coupling-assisted electrocatalysis.

In short, external field regulation has great potential as a new means of regulating electrocatalytic performances and awaits further exploration by researchers. With the ongoing development of research, we can expect to see more studies on the physical field-assisted electrolytic water in the future. The principles behind HER from the electrolytic water under different external fields also merit deeper investigation and interpretation. Moreover, the field-assisted electrocatalytic technology is likely to find applications in fields beyond water splitting.

Acknowledgement

This work was supported by National Natural Science Fund of China (Grant No. 12172118 and 22075211), the Research Program of Local Science and Technology Development under the Guidance of Central (216Z4402G), Science and Technology Project of Hebei Education Department (BJK2022015). We also acknowledge support from ‘‘Yuanguang” Scholar Program of Hebei University of Technology.

Author Contribution: Conceptualization, S. Chen and C.H. An; Formal Analysis, C.L. Qin, S. Chen and H. Gomaa; Investigation, C.L. Qin, S. Chen, Liu, Q. and S. Wu; Writing – Original Draft Preparation, C.L. Qin, S. Chen, C.H. An and S. Wu; Writing – Review & Editing, Q.B. Deng, X.J. Liu, M.A. Shenashen and S.A. El-Safty; Supervision, N. Hu; Funding Acquisition, C.L. Qin, Q.B. Deng and X.J. Liu

References

(1) Zhang, Q.; Lian, K.; Liu, Q.; Qi, G. C.; Zhang, S. S.; Luo, J.; Liu, X. *J. Colloid Interface Sci.* **2023,** *646*, 844. doi: 10.1016/j.jcis.2023.05.074

(2) Li, X.; Li, Z. Q.; Liu, H. Y.; Lu, S. Y. *Rare Metals* **2023,** *42*, 1808. doi: 10.1007/s12598-022-02251-3

(3) Feng, J. X.; Zheng, D.; Yin, R. L.; Niu, X. X.; Xu, X. L.; Meng, S. B.; Ma, S. L.; Shi, W.H.; Wu, F. F.; Liu, W. X., et al. *Small Struct.* **2023,** *4*(7). doi: 10.1002/sstr.202200340

(4) Chen, S. S.; Lian, K.; Liu, W. X.; Liu, Q.; Qi, G. C.; Luo, J.; Liu, X. J. *Nano Res.* **2023.** doi: 10.1007/s12274-023-5798-4.

(5) Xu, Y. L.; Zhang, X. L.; Liu, Y. Y.; Wang, R. J.; Yang, Y. W.; Chen, J. F. *Environ. Sci. Pollut. Res.* **2023,** *30*, 11302. doi: 10.1007/s11356-022-24728-5

(6) Avani, A. V.; Anila, E. I. *Int. J. Hydrog. Energy* **2022,** *47*, 20475. doi: 10.1016/j.ijhydene.2022.04.252

(7) Cui, S. F.; Li, M.; Bo, X. J. *Int. J. Hydrog. Energy* **2020,** *45*, 21221. doi: 10.1016/j.ijhydene.2020.05.006

(8) Hu, C. G.; Dai, L. M. *Adv. Mater.* **2017,** *29*(9). doi: 10.1002/adma.201604942

(9) Ding, J. Y.; Yang, H.; Zhang, S. S.; Liu, Q.; Cao, H. Q.; Luo, J.; Liu, X. J. *Small* **2022,** *18*, e2204524. doi: 10.1002/smll.202204524

(10) Qin, Z. G.; Liu, W. X.; Que, W. B.; Feng, J. X.; Shi, W. H.; Wu, F. F.; Cao, X. H. *ChemPhysMater* **2023,** *2,* 185. doi: 10.1016/j.chphma.2022.11.001

(11) Ge, S. M.; Zhang, L. W.; Hou, J. R.; Liu, S.; Qin, Y. J.; Liu, Q.; Cai, X. B.; Sun, Z. Y.; Yang, M. S.; Luo, J., et al. *ACS Appl. Energ. Mater.* **2022,** *5*, 9487. doi: 10.1021/acsaem.2c01006

(12) Liu, W. X.;Feng, J. X.;Wei, T. R.;Liu, Q.;Zhang, S. S.;Luo, Y.;Luo, J.;Liu, X. J. *Nano Res.* **2022,** *16,* 2325. doi:

10.1007/s12274-022-4929-7

(13) Liu, W. X.; Niu, X. X.; Feng, J. X.; Yin, R. L.; Ma, S. L.; Que, W. B.; Dai, J. L.; Tang, J. W.; Wu, F. F.; Shi, W. H., et al. *ACS Appl. Mater. Interfaces* **2023,** *15,* 15344. doi: 10.1021/acsami.2c21616

(14) Zhu, Y. L.; Tahini, H. A.; Hu, Z. W.; Dai, J.; Chen, Y. B.; Sun, H. N.; Zhou, W.; Liu, M. L.; Smith, S. C.; Wang, H. T., et al. *Nat. Commun.* **2019,** *10*, 149. doi: 10.1038/s41467-018-08117-6

(15) Suryanto, B. H. R.; Wang, Y.; Hocking, R. K.; Adamson, W.; Zhao, C. *Nat. Commun.* **2019,** *10*, 5599. doi: 10.1038/s41467-019-13415-8

(16) Gao, R.; Dai, Q. B.; Du, F.; Yan, D. P.; Dai, L. M. *J. Am. Chem. Soc.* **2019,** *141*, 11658. doi: 10.1021/jacs.9b05006

(17) Han, N. N.; Yang, K. R.; Lu, Z. Y.; Li, Y. J.; Xu, W. W.; Gao, T. F.; Cai, Z.; Zhang, Y.; Batista, V. S.; Liu, W., et al. *Nat. Commun.* **2018,** *9*, 924. doi: 10.1038/s41467-018-03429-z

(18) Shi, H. H.; Liang, H. F.; Ming, F. W.; Wang, Z. C. *Angew. Chem. Int. Ed.* **2017,** *56*, 573. doi: 10.1002/anie.201610211

(19) Xie, J. F.; Xie, Y. *Chem.-Eur. J.* **2016,** *22*, 3588. doi: 10.1002/chem.201501120

(20) Cheng, C.; Chen, W.; Chen, Y.; Chen, Y. H.; Chen, Y.; Ding, F.; Fan, C. H.; Fan, H. J.; Fan, Z. X.; Gong, C., et al. *Acta Phys. Chim. Sin.* **2021,** *37*(12). doi: 10.3866/pku.Whxb202108017

(21) Haider, Z.; Fatima, S.; Zahra, S. A.; Li, H.; Jafri, S. H. M.; Amin, F.; Rizwan, S. *ACS Appl. Nano Mater.* **2023**, 6, 2374. doi: 10.1021/acsanm.2c04428

(22) An, C. H.; Dong, D. D.; Wu, S.; Gao, L. X.; Chen, X. D.; Jiao, P. G.; Deng, Q. B.; Li, J. S.; Hu, N. *Chem. Asian J.* **2023**. doi: 10.1002/asia.202300429

(23) Deng, K.; Zhou, T.; Mao, Q.; Wang, S.; Wang, Z.; Xu, Y.; Li, X.; Wang, H.; Wang, L. *Adv. Mater.* **2022,** *34*(18). doi: 10.1002/adma.202110680

(24) Mishra, S. S.; Kumbhakar, P.; Nellaiappan, S.; Katiyar, N. K.; Tromer, R.; Wollner, C. F.; Galvao, D. S.; Tiwary, C. S.; Ghosh, C.; Dasgupta, A., et al. *Energy Technol.* **2023,** *11*(2). doi: 10.1002/ente.202200860

(25) Deng, K.; Wang, W. X.; Mao, Q. Q.; Yu, H. J.; Wang, Z. Q.; Xu, Y.; Li, X. N.; Wang, H. J.; Wang, L. *Small* **2022,** *18*(32). doi: 10.1002/smll.202203020

(26) Yan, H. L.; Li, P. F.; Liu, X. H.; Chen, S. M. *New J. Chem.* **2021,** *45*, 22758. doi: 10.1039/d1nj04956a

(27) Duan, X. X.; Getaye Sendeku, M.; Zhang, D. M.; Zhou, D. J.; Xu, L. J.; Gao, X. Q.; Chen, A. B.; Kuang, Y.; Sun, X. M. *Acta Phys. Chim. Sin.* **2023,** *40*, 1. doi: 10.3866/pku.Whxb202303055

(28) Guo, J. W.; Wei, Z. J.; Wang, K.; Zhang, H. *Int. J. Hydrog. Energy* **2021,** *46*, 27529. doi: 10.1016/j.ijhydene.2021.06.013

(29) Zhou, Y.; Guo, Q. Y.; Luo, J. B.; Wang, X. Z.; Sun, F. C.; Wang, C. C.; Wang, S. T.; Zhang, J. *Int. J. Hydrog. Energy* **2023,** *48*, 4984. doi: 10.1016/j.ijhydene.2022.11.075

(30) Zhou, Y.; Chen, Y. L.; Wei, M. B.; Fan, H. G.; Liu, X. Y.; Liu, Q. Y.; Liu, Y. M.; Cao, J.; Yang, L. L. *CrystEngComm* **2021,** *23*, 69. doi: 10.1039/d0ce01527j

(31) Yang, X. H.; Feng, Z.; Guo, Z. Y. *Molecules* **2022,** *27*(5). doi: 10.3390/molecules27051528

(32) Butburee, T.; Ponchai, J.; Meeporn, K.; Phawa, C.; Chakthranont, P.; Khemthong, P.; Mano, P.; Namuangruk, S.; Chinsirikul, W.; Faungnawakij, K., et al. *Small* **2022,** *18*(51). doi: 10.1002/smll.202204767

(33) Luo, Y. T.; Zhang, S. Q.; Pan, H. Y.; Xiao, S. J,; Guo, Z. L.; Tang, L.; Khan, U.; Ding, B. F.; Li, M.; Cai, Z. Y., et al. *ACS Nano* **2020,** *14*, 767. doi: 10.1021/acsnano.9b07763

(34) Jiao, P. G.; Ye, D. H,; Zhu, C. Y.; Wu, S.; Qin, C. L.; An, C. H.; Hu, N.; Deng, Q. B. *Nanoscale* **2022,** *14*, 14322. doi: 10.1039/d2nr03687h

(35) Zhang, J. M.; Xu, X. P.; Yang, L.; Cheng, D. J.; Cao, D. P. *Small Methods* **2019,** *3*(12). doi: 10.1002/smtd.201900653

(36) Ma, Y. H.; Leng, D. F.; Zhang, X. M.; Fu, J. J.; Pi, C. R.; Zheng, Y.; Gao, B. A.; Li, X. G.; Li, N.; Chu, P. K., et al. *Small* **2022,** *18*(39). doi: 10.1002/smll.202203173

(37) Liu, W. X.; Que, W.B.; Yin, R. L.; Dai, J. L.; Zheng, D.; Feng, J. X.; Xu, X. L.; Wu, F. F.; Shi, W. H.; Liu, X. J., et al. *Appl. Catal. B Environ.* **2023,** *328*. doi: 10.1016/j.apcatb.2023.122488

(38) Wang, J.; Wei, J. K.; An, C. H.; Tang, H. L.; Deng, Q. B.; Li, J. S. *Hem. Commun.* **2022,** *58*, 10907. doi: 10.1039/d2cc03630d

(39) An, C. H.; Kang, W.; Deng, Q. B.; Hu, N. *Rare Metals* **2021,** *41*, 378. doi: 10.1007/s12598-021-01791-4

(40) Li, K.; Xu, J.; Chen, C.; Xie, Z. Z.; Liu, D.; Qu, D. Y.; Tang, H. L.; Wei, Q.; Deng, Q. B; Li, J. S., et al. *J. Colloid Interface Sci.* **2021,** *582*, 591. doi: 10.1016/j.jcis.2020.08.071

(41) An, C. H.; Wang, Y. C.; Huang, R.; Li, Y. Q.; Wang, C.; Wu, S.; Gao, L. X.; Zhu, C. Y.; Deng, Q. B.; Hu, N. *Colloid Surf. A-Physicochem. Eng. Asp.* **2023,** *667*(20). doi: 10.1016/j.colsurfa.2023.131360

(42) Wang, J. H.; Yan, M. Y.; Zhao, K. N.; Liao, X. B.; Wang, P. Y.; Pan, X. L.; Yang, W.; Mai, L. Q. *Adv. Mater.* **2017,** *29*(7). doi: 10.1002/adma.201604464

(43) Qin, X.; Teng, J.; Guo, W. Y.; Wang, L.; Xiao, S. N.; Xu, Q. J.; Min, Y. L,; Fan, J. C. *Catal. Lett.* **2022,** *153*, 673. doi: 10.1007/s10562-022-04032-0

(44) An, C. H.; Wang, T. Y.; Wang, S. K.; Chen, X. D.; Han, X. P.; Wu, S.; Deng, Q. B.; Zhao, L. B.; Hu, N. *Ultrason. Sonochem.* **2023,** *98*, 106503. doi: 10.1016/j.ultsonch.2023.106503

(45) Zhang, H.; Wei, T. R.; Qiu, Y.; Zhang, S. S.; Liu, Q.; Hu, G. Z.; Luo, J.; Liu, X. J. *Small* **2023,** *19*(16). doi: 10.1002/smll.202207249

(46) Que, H. F.; Jiang, H. N.; Wang, X. G.; Zhai, P. B.; Meng, L. J.; Zhang, P.; Gong, Y. J. *Acta Phys. Chim. Sin.* **2021,** *37*(11). doi: 10.3866/pku.Whxb202010051

(47) Zhu, D. D.; Liu, J. L.; Zhao, Y. Q.; Zheng, Y.; Qiao, S. Z. *Small* **2019,** *15*(14). doi: 10.1002/smll.201805511

(48) Wang, X. M; Zhang, H.; Yang, Z.; Zhang, C.; Liu, S. X. *Ultrason. Sonochem.* **2019,** *59*. doi: 10.1016/j.ultsonch.2019.104714

(49) Zhao, L.; Wen, M.; Tian, Y. K.; Wu, Q. S.; Fu, Y. Q. *J. Energy Chem.* **2022,** *74*, 203. doi: 10.1016/j.jechem.2022.07.017

(50) Zhou, D.; Yin, J. Z. *Nano* **2020,** *15*(10). doi: 10.1142/S1793292020501180

(51) Contreras-Pereda, N.; Moghzi, F.; Baselga, J.; Zhong, H. X.; Janczak, J.; Soleimannejad, J.; Dong, R. H.; Ruiz-Molina, D. *Ultrason. Sonochem.* **2021,** *70*. Doi : 10.1016/j.ultsonch.2020.105292

(52) He, C. H.; Hu, X. C.; Wang, J.; Bu, L. Z.; Zhan, C. H.; Xu, B. Y.; Li, L. G.; Li, Y. C.; Huang, X. Q. *Sci. China-Mater.* **2022,** *65*, 3470. doi: 10.1007/s40843-022-2098-x

(53) Wang, Q.; Wang, S.; Li, J. Y.; Gan, Y. C.; Jin, M. T.; Shi, R.; Amini, A.; Wang, N.; Cheng, C. *Adv. Sci.* **2023,** *10*(3). doi: 10.1002/advs.202205638

(54) Yang, S.; Wu, J.; Wang, C.; Yan, H.; Han, L. Q.; Feng, J. M.; Zhang, B.; Li, D. J.; Yu, G.; Luo, B. R. *Dalton Trans.* **2022,** *51*, 13351. doi: 10.1039/d2dt02066a

(55) Zhu, L. L.; Wang, Z.; Li, C. D.; Li, H.; Huang, Y. A.; Li, H.; Wu, Z. Q.; Lin, S.; Li, N.; Zhu, X. B., et al. *J. Mater. Chem. A* **2022,** *10*, 21013. doi: 10.1039/d2ta05954a

(56) Xiong, G. W.; Chen, Y. K.; Zhou, Z. Q.; Liu, F.; Liu, X. Y.; Yang, L. J.; Liu, Q. L.; Sang, Y. H.; Liu, H.; Zhang, X. L., et al. *Adv. Funct. Mater.* **2021,** *31*(15). doi: 10.1002/adfm.202009580

(57) Solomon, G.; Mazzaro, R.; Morandi, V.; Concina, I.; Vomiero, A. *Crystals* **2020,** *10*(11). doi: 10.3390/cryst10111040

(58) Hu, R.; Jiang, H. Y.; Xian, J. L.; Mi, S. Y.; Wei, L. Y.; Fang, G. Y.; Guo, J. Y.; Xu, S. Q.; Liu, Z. Y.; Jin, H. Y., et al. *Appl. Catal. B-Environ.* **2022,** *317*. doi: 10.1016/j.apcatb.2022.121728

(59) Sarwar, S.; Ali, A.; Liu, Z. Q.; Li, J. H.; Uprety, S.; Lee, H.; Wang, R. G; Park, M. J.; Bozack, M. J.; Adamczyk, A. J., et al. *J. Colloid Interface Sci.* **2021,** *581*, 847. doi: 10.1016/j.jcis.2020.07.122

(60) Rafai, S.; Qiao, C.; Wang, Z. T.; Cao, C. B.; Mahmood, T.; Naveed, M.; Younas, W.; Khalid, S. *ChemElectroChem* **2019,** *6*, 5469. doi: 10.1002/celc.201901363

(61) Zhang, H.; Xiao, X. J.; Xu, H. L.; Wang, L.; Li, Y.; Ouyang, C. Y.; Zhong, S. L. *Nanoscale* **2023,** *15*, 4429. doi: 10.1039/d2nr06184h

(62) Ma, Y.; Wang, F. G.; Fan, R. Y.; Wang, H. Y.; Yu, W. L.; Liu, H. J.; Chi, J. Q.; Wang, L.; Chai, Y. M.; Dong, B. *Int. J. Hydrog. Energy* **2021,** *46*, 35311. doi: 10.1016/j.ijhydene.2021.08.106

(63) Shen, H.; Wei, T. R.; Liu, Q.; Zhang, S. S.; Luo, J.; Liu, X. *J. Colloid Interface Sci.* **2023,** *634*, 730. doi: 10.1016/j.jcis.2022.12.067

(64) Yao, J. D.; Huang, W. J.; Fang, W.; Kuang, M.; Jia, N.; Ren, H.; Liu, D. B.; Lv, C. D.; Liu, C. T.; Xu, J. W., et al. *Small Methods* **2020,** *4*(10). doi: 10.1002/smtd.202000494

(65) Zhang, Q.; Li, P. S.; Zhou, D. J; Chang, Z.; Kuang, Y.; Sun, X. M. *Small* **2017,** *13*(41). doi: 10.1002/smll.201701648

(66) Lu, Z. Y.; Li, Y. J.; Lei, X. D.; Liu, J. F.; Sun, X. M. *Mater. Horizons* **2015,** *2*, 294. doi: 10.1039/c4mh00208c

(67) Su, M. X.; Zhou, W. D.; Liu, L.; Chen, M. Y.; Jiang, Z. Z.; Luo, X. F.; Yang, Y.; Yu, T.; Lei, W.; Yuan, C. L. *Adv. Funct. Mater.* **2022,** *32*(22). doi: 10.1002/adfm.202111067

(68) Li, H.; Liu, S. C.; Liu, Y. *ACS Sustain. Chem. Eng.* **2021,** *9*, 12376. doi: 10.1021/acssuschemeng.1c04735

(69) Zhou, W. D.; Chen, M. Y.; Guo, M. M.; Hong, A. J.; Yu, T.; Luo, X. F.; Yuan, C. L.; Lei, W.; Wang, S. G. *Nano Lett.* **2020,** *20*, 2923. doi: 10.1021/acs.nanolett.0c00845

(70) Zhang, Y. Y.; Guo, P.; Niu, S. Q.; Wu, J.; Wang, W.; Song, B.; Wang, X. J.; Jiang, Z. X.; Xu, P. *Small Methods* **2022,** *6*(6). doi: 10.1002/smtd.202200084

(71) Hu, J.; Du, H. W.; Qu, B.; Jiang, D. C.; Zhu, C. H.; Yuan, Y. P. *Int. J. Hydrog. Energy* **2021,** *46*, 21433. doi: 10.1016/j.ijhydene.2021.03.237

(72) Ding, J. W.; Wang, F. M.; Pan, F.; Yu, P.; Gao, N.; Goldsmith, R. H.; Cai, S. F.; Yang, R.; He, J. *ACS Catal.* **2021,** *11*, 13721. doi: 10.1021/acscatal.1c03811

(73) Li, B. L.; Zou, H. L.; Tian, J. K.; Chen, G.; Wang, X. H.; Duan, H.; Li, X. L.; Shi, Y.; Chen, J. R.; Li, L. J., et al. *Nano Energy* **2019,** *60*, 689. doi: 10.1016/j.nanoen.2019.03.093

(74) Zabelin, D.; Zabelina, A.; Miliutina, E.; Trelin, A.; Elashnikov, R.; Nazarov, D.; Maximov, M.; Kalachyova, Y.; Sajdl, P.; Lancok, J., et al. *Chem. Eng. J.* **2022,** *443*. doi: 10.1016/j.cej.2022.136440

(75) Zabelina, A.; Zabelin, D.; Miliutina, E.; Lancok, J.; Svorcik, V.; Chertopalov, S.; Lyutakov, O. *J. Mater. Chem. A* **2021,** *9*, 17770. doi: 10.1039/d1ta04505a

(76) Zabelina, A.; Miliutina, E.; Zabelin, D.; Burtsev, V.; Buravets, V.; Elashnikov, R.; Neubertova, V.; Šťastný, M.; Popelková, D.; Lancok, J., et al. *Chem. Eng. J.* **2023,** *454*. doi: 10.1016/j.cej.2022.140441

(77) Liang, H. Y.; Xi, H. J.; Liu, S. Q.; Zhang, X. M.; Liu, H. Q. *Nanoscale* **2019,** *11*, 18183. doi: 10.1039/c9nr06222j

(78) Chang, B.; Ai, Z. Z.; Shi, D.; Zhong, Y. Y.; Zhang, K.; Shao, Y. L.; Zhang, L.; Shen, J. X.; Wu, Y. Z.; Hao, X. P. *J. Mater. Chem. A* **2019,** *7*, 19573. doi: 10.1039/c9ta06589j

(79) Deng, L. Q.; Chang, B.; Shi, D.; Yao, X. G.; Shao, Y. L.; Shen, J. X.; Zhang, B. G.; Wu, Y. Z.; Hao, X. P. *Renew. Energy* **2021,** *170*, 858. doi: 10.1016/j.renene.2021.02.040

(80) Lee, J. Y.; Kang, S.; Lee, D.; Choi, S.; Yang, S.; Kim, K.; Kim, Y. S.; Kwon, K. C.; Choi, S. H.; Kim, S. M., et al. *Nano Energy* **2019,** *65*. doi: 10.1016/j.nanoen.2019.104053

(81) Yan, Y. B.; Zhai, D.; Liu, Y.; Gong, J.; Chen, J.; Zan, P.; Zeng, Z. P.; Li, S. Z.; Huang, W.; Chen, P. *ACS Nano* **2020,** *14*, 1185. doi: 10.1021/acsnano.9b09554

(82) Perivoliotis, D. K.; Stangel, C.; Sato, Y.; Suenaga, K.; Tagmatarchis, N. *2D Mater.* **2022,** *10*(1). doi: 10.1088/2053-1583/ac9290

(83) Meng, H. Y.; Xi, W.; Ren, Z. Y.; Du, S. C.; Wu, J.; Zhao, L.; Liu, B. W.; Fu, H. G. *Appl. Catal. B-Environ.* **2021,** *284*, doi: 10.1016/j.apcatb.2020.119707

(84) Chung, C. C.; Yeh, H.; Wu, P. H.; Lin, C. C.; Li, C. S.; Yeh, T. T.; Chou, Y.; Wei, C. Y.; Wen, C. Y.; Chou, Y. C., et al. *ACS Nano* **2021,** *15*, 4627. doi: 10.1021/acsnano.0c08970

(85) Ai, L. H.; Li, N.; Chen, M.; Jiang, H. L.; Jiang, J. *J. Mater. Chem. A* **2021,** *9*, 16479. doi: 10.1039/d1ta02995a

(86) Zhang, Y.; Hu, L.; Zhang, Y. C.; Wang, X. Z.; Wang, H. G. *Appl. Catal. B-Environ.* **2022,** *315*, doi: 10.1016/j.apcatb.2022.121540

(87) Liang, Y. G.; Zhang, Y. J.; Wang, X. K.; Zhou, J.; Cao, Z. W.; Huang, M. H.; Jiang, H. Q. *Mater. Today Energy* **2022,** *25*, doi: 10.1016/j.mtener.2022.100966

(88) Gu, L.; Zhang, C.; Guo, Y. M.; Gao, J.; Yu, Y. F.; Zhang, B. *ACS Sustain. Chem. Eng.* **2019,** *7*, 3710. doi: 10.1021/acssuschemeng.8b06117

(89) Lv, X. S.; Wei, W.; Zhao, P.; Er, D. Q.; Huang, B. B.; Dai, Y.; Jacob, T. *J. Catal.* **2019,** *378*, 97. doi: 10.1016/j.jcat.2019.08.019

(90) Wang, L. F.; Shan, Y.; Liu, L. Z. *Mater. Chem. Phys.* **2020,** *239*. doi: 10.1016/j.matchemphys.2019.122046

(91) Deng, Q. B.; Huang, R.; Shao, L. H.; Mumyatov, A. V.; Troshin, P. A.; An, C. H.; Wu, S.; Gao, L. X.; Yang, B.; Hu, N. *Phys. Chem. Chem. Phys.* **2023,** *25*, 12565. doi: 10.1039/d3cp01077e

(92) Yang, Z. Y.; Zhu, J.; Xu, X. L.; Wang, L.; Zhou, G. B.; Yang, Z.; Zhang, Y. F. *RSC Adv.* **2023,** *13*, 4056. doi: 10.1039/d2ra07363c

(93) Liao, M. S.; Zhu, Q. M.; Li, S. H.; Li, Q. Q.; Tao, Z. T.; Fu, Y. C. *Nano Res.* **2022**, *16*, 5419. doi: 10.1007/s12274-022-5170-0

(94) Wang, L.; Zeng, Z. H.; Gao, W. P.; Maxson, T.; Raciti, D.; Giroux, M.; Pan, X. Q.; Wang, C.; Greeley, J. *Science* **2019,** *363*, 870. doi: 10.1126/science.aat8051

(95) Li, A. J.; Hao, Y. Z.; Feng, G.; Zhong, X. L. *Catal. Sci. Technol.* **2022,** *12*, 1458. doi: 10.1039/d1cy00261a

(96) Wu, G.; Han, X.; Cai, J. Y.; Yin, P. Q.; Cui, P. X.; Zheng, X. S.; Li, H.; Chen, C.; Wang, G. M.; Hong, X. *Nat. Commun.* **2022,** *13*(1). doi: 10.1038/s41467-022-31971-4

(97) Guo, K.; Han, X.; Wei, S. Y.; Bao, J. C.; Lin, Y.; Li, Y. F.; Xu, D. D. *Nano Lett.* **2023,** *23*, 1085. doi: 10.1021/acs.nanolett.2c04729

(98) Lv, F.; Huang, B. L.; Feng, J. R.; Zhang, W. Y.; Wang, K.; Li, N.; Zhou, J. H.; Zhou, P.; Yang, W. X.; Du, Y. P., et al. *Natl. Sci. Rev.* **2021,** *8*(9). doi: 10.1093/nsr/nwab019

(99) Wang, Y.; Yang, C. X.; Li, Z. M.; Liang, Z. Z.; Cao, G. Z. *Small* **2020,** *16*(25). doi: 10.1002/smll.202001973

(100) Qi, K.; Cui, X. Q.; Gu, L.; Yu, S. S.; Fan, X. F.; Luo, M. C.; Xu, S.; Li, N. B.; Zheng, L. R.; Zhang, Q. H., et al. *Nat. Commun.* **2019,** *10, 1*. doi: 10.1038/s41467-019-12997-7

(101) Nguyen, D. N.; Phu, T. K. C.; Kim, J.; Hong, W. T.; Kim, J. S.; Roh, S. H.; Park, H. S.; Chung, C. H.; Choe, W. S.; Shin, H., et al. *Small* **2022,** *18*(45). doi: 10.1002/smll.202204797

(102) Deng, Q. B.; Jia, H. X.; An, C. H.; Wu, S.; Zhao, S.; Hu, N. *Compos. Pt. A-Appl. Sci. Manuf.* **2023,** *165*. doi: 10.1016/j.compositesa.2022.107336

(103) Meng, G.; Sun, W. M.; Mon, A. A.; Wu, X.; Xia, L. Y.; Han, A. J.; Wang, Y.; Zhuang, Z. B; Liu, J. F; Wang, D. S., et al. *Adv. Mater.* **2019,** *31*(37). doi: 10.1002/adma.201903616

(104) Wang, C.; An, C. H.; Qin, C. L.; Gomaa, H.; Deng, Q. B.; Wu, S.; Hu, N. *Nanomaterials* **2022,** *12*(14). doi: 10.3390/nano12142480

(105) Shi, Z. K.; Yu, Z. B.; Guo, J.; Jiang, R. H.; Hou, Y. P.; Chen, Y. S.; Chen, H. L.; Wang, M.; Pang, H.; Tang, W. J. *Nanoscale* **2022,** *14*, 1370. doi: 10.1039/d1nr07438e

(106) Jansonius, R. P.; Schauer, P. A.; Dvorak, D. J.; MacLeod, B. P.; Fork, D. K.; Berlinguette, C. P. *Angew. Chem. Int. Ed.* **2020,** *59*, 12192. doi: 10.1002/anie.202005248

(107) Huang, T.; Si, Y.; Wu, H. Y.; Xia, L. X.; Lan, Y.; Huang, W. Q.; Hu, W. Y.; Huang, G. F. *Chin. Phys. B* **2021,** *30*(2). doi: 10.1088/1674-1056/abbbe7

(108) Wei, Y. H.; Gao, F.; Huang, H. C.; Jiang, G. *Int. J. Hydrog. Energy* **2022,** *47*, 8338. doi: 10.1016/j.ijhydene.2021.12.210

(109) Li, F. F.; Ai, H. Q.; Liu, D.; Lo, K. H.; Pan, H. *J. Mater. Chem. A* **2021,** *9*, 17749. doi: 10.1039/d1ta03412j

(110) Gao, X. P.; Zhou, Y. N.; Tan, Y. J.; Liu, S. Q.; Cheng, Z. W.; Shen, Z. W. *Phys. Chem. Chem. Phys.* **2020,** *22*, 2457. doi: 10.1039/c9cp05548g

(111) Gu, Y. T.; Wei, B.; Legut, D.; Fu, Z. H.; Du, S. Y.; Zhang, H. J.; Francisco, J. S.; Zhang, R. F. *Adv. Funct. Mater.* **2021,** *31*(43). doi: 10.1002/adfm.202104285

(112) Liu, W. W.; Kong, Y. C.; Wang, B.; Li, X. S.; Liu, P. F.; Santiago, A. R. P.; He, T. W. *Nanomaterials* **2021,** *11*(12). doi: 10.3390/nano11123173

(113) Liang, D.; Zhang, Y. W.; Lu, P. F.; Yu, Z. G. *Nanoscale* **2019,** *11*, 18329. doi: 10.1039/c9nr06541e

(114) Wang, W. Y.; Meng, J.; Hu, Y. J.; Wang, J. J.; Li, Q. X.; Yang, J. L. *J. Mater. Chem. A* **2022,** *10*, 9848. doi: 10.1039/d2ta00547f

(115) Kong, Y. C.; Ai, H. Q.; Wang, W.; Xie, X. H.; Lo, K. H.; Wang, S. P.; Pan, H. *ACS Appl. Nano Mater.* **2020,** *3*, 2804. doi: 10.1021/acsanm.0c00119

(116) Lou, H.; Chen, W.; Yu, G. T.; Yang, G. C. *Nanoscale* **2022,** *14*, 3069. doi: 10.1039/d1nr06443f

(117) Zhao, Z. W.; Liu, C. M.; Tsai, H. S.; Zhou, J. M.; Zhang, Y. Q.; Wang, T. Q.; Ma, G. L.; Qi, C. H.; Huo, M. X. *Int. J. Hydrog. Energy* **2022,** *47*, 37429. doi: 10.1016/j.ijhydene.2021.07.117

(118) Zhai, L. L.; She, X. J.; Zhuang, L. C.; Li, Y. Y.; Ding, R.; Guo, X. Y.; Zhang, Y. Q.; Zhu, Y.; Xu, K.; Fan, H. J., et al. *Angew. Chem. Int. Ed.* **2022,** *61*(14). doi: 10.1002/anie.202116057

(119) He, Y. M.; He, Q. Y.; Wang, L. Q.; Zhu, C.; Golani, P.; Handoko, A. D.; Yu, X. C.; Gao, C. T.; Ding, M. N.; Wang, X. W., et al. *Nat. Mater.* **2019,** *18*, 1098. doi: 10.1038/s41563-019-0426-0

(120) Wu, Y. C.; Ringe, S.; Wu, C. L.; Chen, W.; Yang, A. K.; Chen, H.; Tang, M.; Zhou, G. M; Hwang, H. Y.; Chan, K. R., et al. *Nano Lett.* **2019,** *19*, 7293. doi: 10.1021/acs.nanolett.9b02888

(121) Zhang, W. C.; Liao, X. B.; Pan, X. L.; Yan, M. Y.; Li, Y. X.; Tian, X. C.; Zhao, Y.; Xu, L.; Mai, L. Q. *Small* **2019,** *15*(31). doi: 10.1002/smll.201900964

(122) Wang, Y.; Udyavara, S.; Neurock, M.; Frisbie, C. D. *Nano Lett.* **2019,** *19*, 6118. doi: 10.1021/acs.nanolett.9b02079

(123) Zhu, X. H.; Wang, C. Y.; Wang, T. L.; Lan, H. H.; Ding, Y.; Shi, H.; Liu, L. S.; Shi, H. W.; Wang, L. Y.; Wang, H. L., et al. *Adv. Mater.* **2022,** *34*(27). doi: 10.1002/adma.202202479

(124) Huang, J. Z; Zhuang, Z. C.; Zhao, Y.; Chen, J. Q.; Zhuo, Z. W.; Liu, Y. W.; Lu, N.; Li, H. Q.; Zhai, T. Y. *Angew. Chem. Int. Ed.* **2022,** *61*(32). doi: 10.1002/anie.202203522

(125) Chen, J. Q.; Lu, N.; Zha.o, Y.; Huang, J. Z.; Gan, X. J.; Chen, X. Z.; Yang, Z. H.; Wen, Q. L.; Zhai, T. Y.; Liu, Y. W. *Nano Lett.* **2022,** *22*, 10154. doi: 10.1021/acs.nanolett.2c04087

(126) Wang, Z. G.; Wu, H. H.; Li, Q.; Besenbacher, F.; Li, Y. R.; Zeng, X. C.; Dong, M. D. *Adv. Sci.* **2020,** *7*(3). doi: 10.1002/advs.201901382

(127) Pan, Y. H.; Wang, X. Z.; Zhang, W.Y.; Tang, L. Y.; Mu, Z. Y.; Liu, C.; Tian, B. L.; Fei, M. C; Sun, Y. M.; Su, H. H., et al. *Nat. Commun.* **2022,** *13*(1). doi: 10.1038/s41467-022-30766-x

(128) Wan, T. L.; Liu, J. X.; Tan, X.; Liao, T.; Gu, Y. T.; Du, A. J.; Smith, S.; Kou, L. Z. *J. Mater. Chem. A* **2022,** *10*, 22228. doi: 10.1039/d2ta04464a

(129) Nedrygailov, II; Moon, S. Y.; Park, J. Y. *Sci. Rep.* **2019,** *9*(1). doi: 10.1038/s41598-019-42566-3

(130) Qu, J.; Li, Y.; Li, F.; Li, T. M.; Wang, X. Y.; Yin, Y.; Ma, L. B; Schmidt, O. G.; Zhu, F. *ACS Nano* **2022,** *16*, 2921. doi: 10.1021/acsnano.1c10030

(131) Bian, J. J.; Sun, C. W. *Catal. Sci. Technol.* **2020,** *10*, 6180. doi: 10.1039/c9cy02611h

(132) Ghosh, R.; Singh, M.; Chang, L. W.; Lin, H. I.; Chen, Y. S.; Muthu, J.; Papnai, B.; Kang, Y. S.; Liao, Y. M.; Bera, K. P., et al. *ACS Nano* **2022,** *16*, 5743. doi: 10.1021/acsnano.1c10772

(133) Ghosh, R.; Papnai, B.; Chen, Y. S.; Yadav, K.; Sankar, R.; Hsieh, Y. P.; Hofmann, M.; Chen, Y. F. *Adv. Mater.* **2023,** *35*(16). doi: 10.1002/adma.202210746

(134) Bhartiya, P. K.; Bangruwa, N.; Mishra, D. *MRS Commun.* **2022,** *12*, 745. doi: 10.1557/s43579-022-00223-3

(135) Gao, Y. D.; Bai, L.; Zhang, X.; Yang, F. C. *ChemElectroChem* **2021,** *8*, 2087. doi: 10.1002/celc.202100464

(136) Ma, Q.; Qiao, H.; Huang, Z. Y.; Liu, F.; Duan, C. G.; Zhou, Y.; Liao, G. C.; Qi, X. *Appl. Surf. Sci.* **2021,** *562*, doi: 10.1016/j.apsusc.2021.150213

(137) Zhang, D. X.; Dong, W. X.; Liu, Y. H.; Gu, X. Q.; Yang, T. Y.; Hong, Q.; Li, D.; Zhang, D. Q.; Zhou, H. B.; Huang, H., et al. *ACS Appl. Mater. Interfaces* **2021,** *13*, 42125. doi: 10.1021/acsami.1c09948

(138) Farahi, M.; Fathirad, F.; Shamspur, T.; Mostafavi, A. *Mater. Chem. Phys.* **2023,** *293*(1). doi: 10.1016/j.matchemphys.2022.126941

(139) Bai, L.; Jia, S. J.; Gao, Y. D.; Li, C.; Chen, X.; Zhou, S.; Han, J. W.; Yang, F. C.; Zhang, X.; Lu, S. Y. *Energy Environ. Mater.* **2023**, doi: 10.1002/eem2.12456

(140) Shenashen, M.A.; Hassen, D.; El-Safty, S.A.; Isago, H.; Elmarakbi, A.; Yamaguchi, H. *Chem. Eng. J.* **2017**, *313*, 83. doi: 10.1016/j.cej.2016.12.003

(141) Hassen, D.; El-Safty, S.A.; Tsuchiya, K.; Chatterjee, A.; Elmarakbi, A.; Shenashen, M.A.; Sakai, M. *Sci. Rep.*, **2016**, *6*, 24330. doi: 10.1038/srep24330

(142) Shenashen, M.A.; Hassen, D.; El-Safty, S.A.; Selim, M.M.; Akhtar, N.; Chatterjee, A.; Elmarakbi, A. *Adv. Mater. Interfaces*, **2016**, *3(24)*, 1600743. doi :10.1002/admi.201600743

(143) Hassen, D.; Selim, M.M.; El-Safty, S.A.; Khalil, K.A.; Abu El-Maged, G.; Dewidar, M. *Nano-Structures & Nano-Objects*, **2017**, *9*, 31. doi: 10.1016/j.nanoso.2016.12.004

(144) Hassen, D.; Shenashen, M.A.; El-Safty, A.R.; Elmarakbi, A.; El-Safty, S.A. *Sci. Rep.*, **2018**, *8*, 3740. doi: 10.1038/s41598-018-21878-w

(145) Hassen, D.; Shenashen, M.A.; El-Safty, S.A.; Selim, M.M.; Isago, H.; Elmarakbi, A.; El-Safty, A.; Yamaguchi, H. *J. Power Sources*, **2016**, *330*, 292. doi: 10.1016/j.jpowsour.2016.08.140

(146) Hassan, D.K.; El-Safty, S.A.; Khalil, K.A.; Dewidar, M.; Abu El-Maged, G. Int. *J. Electrochem. Sci.*, **2016**, *11*, 8374. doi: 10.20964/2016.10.09

(147) Hassan, D.; El-Safty, S.A.; Khalil, K.A.; Dewidar, M.; Abu El-magd, G. *Materials*, **2016**, *9*, 759. doi: 10.3390/ma9090759

Graphical Abstract

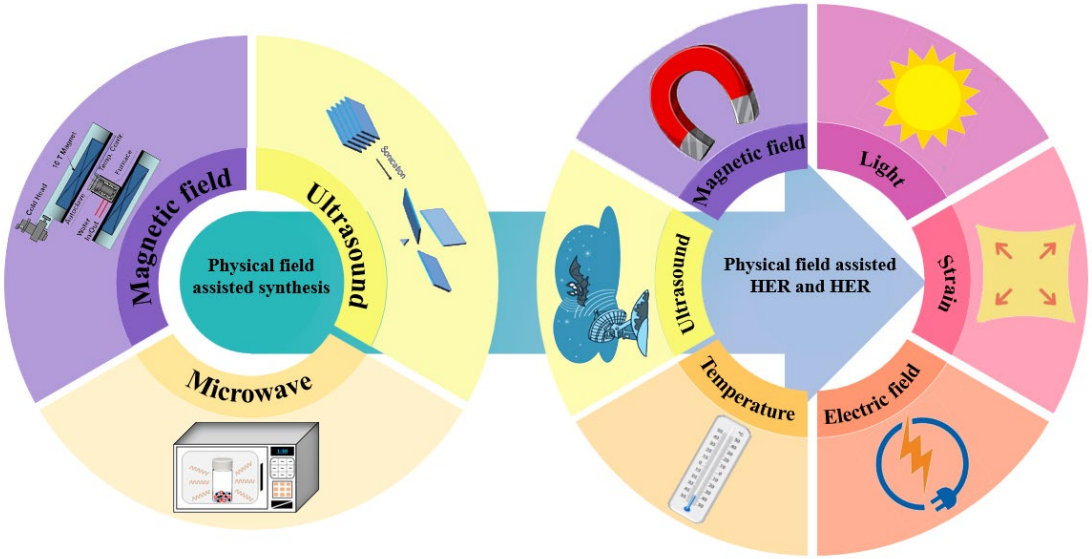

The present strategies for the physical field-assisted synthesis and electrocatalytic processes of 2D electrocatalysts have been summarized in order to give the reader new insights.